Microstructure Measurements from an Underwater Glider in the Turbulent Faroe Bank Channel Overflow

ILKER FER, ALGOT K. PETERSON, AND JENNY E. ULLGREN

Geophysical Institute, University of Bergen, Bergen, Norway

(Manuscript received 25 October 2013, in final form 14 January 2014)

ABSTRACT

Measurements of ocean microstructure are made in the turbulent Faroe Bank Channel overflow using a turbulence instrument attached to an underwater glider. Dissipation rate of turbulent kinetic energy ε is measured using airfoil shear probes. A comparison is made between 152 profiles from dive and climb cycles of the glider during a 1-week mission in June 2012 and 90 profiles collected from the ship using a vertical microstructure profiler (VMP). Approximately one-half of the profiles are collocated. For 96% of the dataset, measurements are of high quality with no systematic differences between dives and climbs. The noise level is less than 5×10^{-11} W kg^{-1}, comparable to the best microstructure profilers. The shear probe data are contaminated and unreliable at the turning depth of the glider and for $U/u_t < 20$, where U is the flow past the sensor, $u_t = (\varepsilon/N)^{1/2}$ is an estimate of the turbulent velocity scale, and N is the buoyancy frequency. Averaged profiles of ε from the VMP and the glider agree to better than a factor of 2 in the turbulent bottom layer of the overflow plume, and beneath the stratified and sheared plume–ambient interface. The glider average values are approximately a factor of 3 and 9 times larger than the VMP values in the layers defined by the isotherms 3°–6° and 6°–9°C, respectively, corresponding to the upper part of the interface and above. The discrepancy is attributed to a different sampling scheme and the intermittency of turbulence. The glider offers a noise-free platform suitable for ocean microstructure measurements.

1. Introduction

Underwater gliders are extensively utilized for hydrographic and biogeochemical observations in the interior ocean (Davis et al. 2003; Rudnick et al. 2004; Beaird et al. 2012; L'Heveder et al. 2013). While the fundamental concept is an infrastructure of coordinated, extended deployments for near-real-time and feasible ocean monitoring, underwater gliders (gliders) offer a platform for intensive process studies. A complementary sampling scheme to that of shipboard measurements improves the spatial and temporal coverage during a research cruise. In particular, the gliders provide an attractive low-noise platform for turbulence measurements because of their buoyancy-driven motion independent of propellers and other mechanical vibration sources (Wolk et al. 2009).

Conventionally, ocean microstructure is measured by loosely tethered vertical profilers equipped with shear probes and/or fast thermistors, sampling the dissipation subrange of the turbulence spectrum (Lueck et al. 2002). Fluxes are then inferred from shear, conductivity, or temperature variances resolved at dissipative scales. Results from a recent test flight of a glider carrying turbulence sensors show that the shear probes are able to resolve turbulent dissipation rates as low as those achieved by the best free-fall microstructure profilers (Wolk et al. 2009). Encouraged by this result, we have incorporated a glider program into our Faroe Bank Channel (FBC) overflow mixing experiment, to sample dissipation rates in the turbulent interface between the dense gravity current and the ambient Atlantic water layer.

The Faroe Bank Channel, with a sill depth of 840 m, is one of the two main passages across the Greenland–Scotland Ridge (GSR), where the deep and intermediate water masses in the Nordic seas flow into the North Atlantic. The bottom-attached overflow plume of dense, cold water flowing out of the FBC is very turbulent with a vertical structure composed of an approximately 100-m-thick turbulent bottom layer (BL) beneath a

Denotes Open Access content.

Corresponding author address: Ilker Fer, Geophysical Institute, University of Bergen, Allégaten 70, 5007 Bergen, Norway.
E-mail: ilker.fer@gfi.uib.no

DOI: 10.1175/JTECH-D-13-00221.1

100-m-thick turbulent, sheared, and stratified interfacial layer (IL) below ambient water (Fer et al. 2010). The location and intensity of turbulent mixing of the overflow plume has an important impact on the ventilation of deep ocean and the oceanic meridional heat transport. An improved understanding and observation-based parameterizations are needed to better represent entrainment and mixing in climate models for credible projections (Legg et al. 2009). Despite its importance, direct turbulence measurements in the region are scarce. Using turbulence measurements from a tethered microstructure profiler, Fer et al. (2010) observed dissipation rates of turbulent kinetic energy, ε, reaching $10^{-5}\,\mathrm{W\,kg^{-1}}$ in both the BL and the IL. The vigorous turbulence near the bottom was due to stirring by the bottom shear stress, estimated to be 2.1 ± 0.2 Pa. The stress in the IL was relatively weak; the enhanced mixing in the IL was attributed to shear instabilities and breaking of internal waves. Beaird et al. (2012) analyzed a large dataset from Seaglider deployments over 3 years around the GSR, and inferred dissipation from finescale vertical velocity and density measurements. Their method was based on a scaling of the turbulent kinetic energy (TKE) equation, and related the energy loss at viscous scales to the energy in the larger energy-containing scales. Results from one Seaglider coordinated with the microstructure survey of Fer et al. (2010) agreed with the shipboard measurements to within a factor of 2. A factor of 2 is considered a good comparison for mixing measurements that often cover several orders of magnitude (see, e.g., MacKinnon et al. 2013).

In this paper, we report on microstructure measurements from a glider deployed in the FBC in early June 2012 and compare shear probe turbulence measurements to more conventional shipboard measurements from a loosely tethered microstructure profiler. Shear probes are the best method for accurate turbulent energy dissipation measurements; all the other methods either require numerous additional assumptions and/or use measurements made at scales larger than the microscale. Dissipation measurements using the temperature gradient microstructure will be a topic for a separate paper. The motivation in using the glider as a platform is the potential for an increased spatial and temporal coverage, supplementing the shipboard measurements. Furthermore, if successful, future deployments using multiple gliders equipped with turbulence sensors can allow for efficient mapping of ocean mixing and contribute to expanding the ocean microstructure datasets, not only in overflow regions but globally.

Our study builds on the proof-of-concept study of Wolk et al. (2009) by utilizing a deep glider in a more realistic and challenging oceanographic setting, and a thorough analysis including a comparison with shipboard microstructure measurements. Our study adds to that of Beaird et al. (2012) by utilizing another type of glider and by making direct microstructure measurements using shear probes. Because the method of turbulence measurements from a glider is not previously documented, emphasis is put on data processing description, quality control, influence of flight behavior on measurements, sources of noise, and comparison with the vertical profiling. The glider and the turbulence package are described in section 2, followed by a deployment overview (section 3), and details of data processing for the glider, the turbulence package, and the vertical microstructure profiler (section 4). Subsequently, results are presented and discussed (section 5), including the flight behavior of the glider, data screening and quality, spectral description of the glider microstructure data, comparisons with the vertical microstructure profiler, and the intermittency of turbulence. An appendix details possible noise sources for the shear probes.

2. Glider and turbulence package

Gliders are autonomous underwater vehicles that move vertically in the ocean by adjusting their buoyancy and center of gravity. As the glider ascends or descends, the wings and tail fin drive a forward motion by translating vertical velocity into horizontal velocity, leading to a sawtooth pattern. The glider utilized in this study is a 1000-m-rated Teledyne Webb Research (TWR) Slocum electric glider (Jones et al. 2005), named Gnå after a goddess in Norse mythology. The glider was ballasted in a laboratory tank with seawater with properties comparable to the deployment site.

During its flight, the glider makes adjustments in heading, pitch, and roll. To adjust headings to predefined way points, a rudder on the tail fin is activated when necessary. The center battery is adjustable: it is moved back and forth (servo control) to adjust pitch and rotated to adjust roll. The recommended pitch angle for the best endurance is $\pm 26°$, that is, vertical-to-horizontal glide ratios of approximately 1:4.

The sensors on the glider include an integrated Sea-Bird Electronics (SBE) conductivity–temperature–depth (CTD) system (SBE-41, unpumped); an attitude sensor measuring heading, pitch, and roll [tilt-compensated three-axis compass module (TCM3), PNI Sensor Corporation]; a navigation pressure sensor (Micron Instruments, MP50-2000), and an altimeter (AIRMAR Technology Corporation, 100-m range). The unpumped CTD does not degrade our measurements or affect our results because the salinity–temperature relation in the Faroe Bank Channel is tight, and the density variability is typically

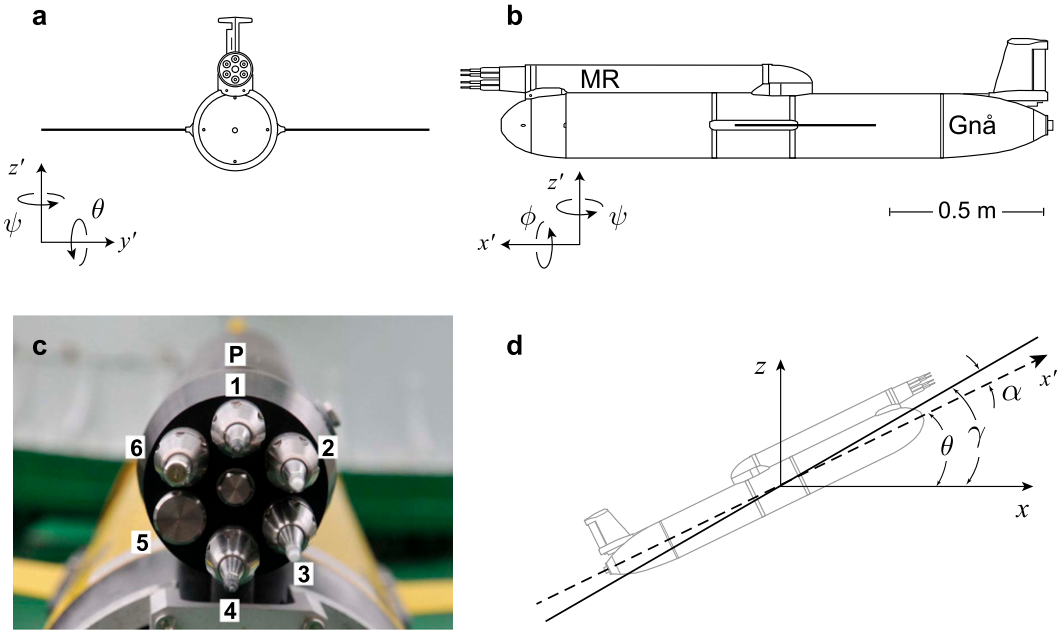

FIG. 1. Illustrations to scale of the glider (Gnå) equipped with the MR seen (a) head on, (b) from the side when level, and (d) from the side during a climb. The coordinate system and various angles are defined in the text, and yaw is ψ. (c) A close-up image of the sensors on the MR. Sensors 1 and 4 are FP07 thermistors, and sensors 2 and 3 are SPM-38 turbulence-shear probes. Slot 5 is not in use and 6 is an LED on/off indicator. The letter P indicates the hole for the pressure sensor, located behind the other sensors.

dominated by temperature. When at the surface, an air bladder located in the aft inflates, exposing the global positioning system (GPS) receiver and Iridium antennas to air. Two-way communication is then established through the Iridium satellite telemetry, or with a FreeWave 900-MHz radio, when the glider is within range of the antenna.

The glider is fitted with a neutrally buoyant, low-power, self-contained turbulence instrument package MicroRider-1000LP (MR), manufactured by Rockland Scientific International. The MR is attached to the top of the glider (Fig. 1). It is powered by the glider's battery but stores data independently on a 16-GB compact flash memory card. The vertical axis-to-axis separation between the glider and the MR is approximately 16 cm. All turbulence sensors protrude horizontally, about 17 cm from the nose of the glider, outside the region of flow deformation. No probe guard is installed. The servo-controlled battery positioning creates vibrations that may affect the quality of turbulence measurements (Wolk et al. 2009). In our deployment, we deactivated the servo control by fixing the center battery pack position in order to reduce the noise in turbulence measurements (see section 3).

The MR is equipped with two airfoil velocity shear probes (SPM-38), two fast-response thermistors (FP07), a pressure transducer, a two-axis vibration sensor (a pair of piezo-accelerometers), and a high-accuracy dual-axis inclinometer (ADIS 16209, pitch and roll angles accurate to 0.1°). The MR also samples the signal plus signal derivative on the thermistor and pressure transducer, and the derivative for shear signals allowing high-resolution measurements (Mudge and Lueck 1994). The sampling rate is 512 Hz on all turbulence channels (vibration, shear, and temperature) and 64 Hz for the other channels (pitch, roll, and pressure).

A right-handed Cartesian coordinate system is used throughout with x' pointing forward along the major axis of the instrument, y' pointing to port, and z' pointing upward. Accordingly, pitch (θ, rotation about the y' axis) is positive when the nose is down, and roll (ϕ, rotation about the x' axis) is positive when the instrument rolls port side up. Note that for nonzero values of pitch and roll, the vertical axis is not aligned with the gravity, g. The shear probes are mounted orthogonal to each other to measure the $\partial w/\partial x'$ and $\partial v/\partial x'$ shear components. In the following, for simplicity, we drop the primes and denote all along-axis gradients (approximately along-path for small angles of attack) with $\partial/\partial x$.

3. Deployment

A research cruise was undertaken on board the Research Vessel *Håkon Mosby* to study the mixing of the

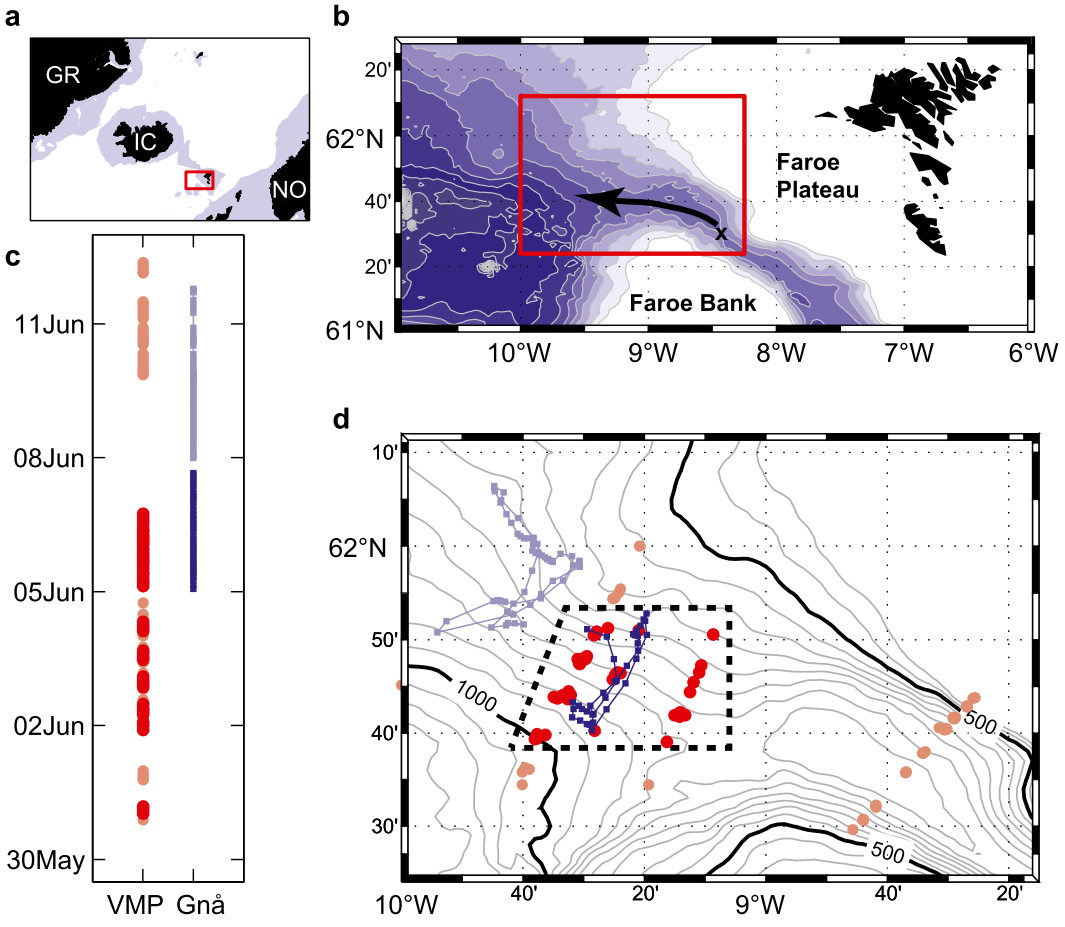

FIG. 2. Location map and the deployment region. (a) Site relative to Norway (NO), Iceland (IC), and Greenland (GR). Depths shallower than 500 m are shaded gray to emphasize the GSR. (b) The region of the red rectangle from (a) is enlarged. Isobaths near the Faroese Islands drawn at 100-m intervals from Smith and Sandwell (1997). Depths shallower than 400 m are masked in white. The saddle point (the ×) near the right bottom of the rectangle, the FBC overflow (arrow), and the borders (red rectangle) of the station map are indicated. (c) Deployment times of the glider (blue) and the VMP (red). (d) Station map showing the VMP stations (red) and the position of the glider before each dive (blue). Paler colors in (c) are used for the stations–dives outside the dashed box. Isobaths (400 m and deeper, at 50-m intervals) are from the high-resolution bathymetry compiled by Simonsen et al. (2002). The area marked by the dashed lines shows the region where a subset of VMP and the glider data are approximately collocated.

FBC overflow. The field work was conducted between 26 May and 14 June 2012, including detailed measurements of hydrography, microstructure, and currents. Full-depth hydrography and horizontal current measurements were made from the ship's CTD rosette equipped with a SBE 911plus CTD and a lowered acoustic Doppler current profiler system. Full-depth vertical microstructure profiles were made by deploying the loosely tethered vertical microstructure profiler VMP2000 (VMP, Rockland Scientific International). Additionally, two TWR deep Slocum gliders were deployed, each equipped with an SBE-41 CTD, and one (Gnå) equipped with the turbulence package MR (section 2). In this paper, only the measurements from the VMP and Gnå are reported; turbulence measurements from the glider are compared to the vertical microstructure profiler data.

The overflow plume at the measurement site is characterized by energetic 3–4-day-period oscillations in plume thickness (Darelius et al. 2011), reflected in the thickness of the turbulent layer (Seim and Fer 2011) and elevated sea level variability and eddy kinetic energy (Høyer and Quadfasel 2001; Darelius et al. 2013). During the collection of data, and also in the following analysis, care was taken to ensure that sufficient sampling and averaging were made over several phases of the oscillations. A station map is shown in Fig. 2 together with the relative time of deployments of the VMP and the glider. Studies utilizing the other datasets collected during the cruise, describing the hydrographic composition,

mesoscale variability, the turbulent structure, and dynamics of the overflow plume, are reported elsewhere (e.g., Darelius et al. 2013; Ullgren et al. 2014).

The VMP is equipped with a pumped SBE conductivity–temperature (C–T) system, and high-resolution sensors for microconductivity (SBE7), temperature (FP07), airfoil shear probes, and a three-axis accelerometer. The turbulence sensors are located at the front of the instrument, protected by a probe guard. The VMP samples the signal plus signal derivative on the thermistor, microconductivity, and pressure transducer, and derivative for shear signals. The sampling rate is 512 Hz for the turbulence channels and 64 Hz for the slow [C, T, pressure (P)] channels. Data are transmitted in real time to a shipboard data acquisition system. During the cruise, the VMP was deployed using a hydraulic winch (Sytech Research Ltd.) with a line-puller system, allowing the instrument to fall freely with a nominal fall rate of about 0.6 m s^{-1}. A total of 90 microstructure profiles were collected between 31 May and 13 June from the surface to approximately 10–30 m above the seabed. Occasionally, in 13 out of 90 casts, the VMP landed on the seabed; 45 casts were within the area identified in Fig. 2d, approximately collocated with the glider (with a mean horizontal separation of 8 km).

Data were recovered from the glider after a mission between 0030 UTC 5 June 2012 and 2000 UTC 11 June 2012. During the first dive, the servo-controlled battery position is used to determine the positions needed to maintain approximately ±26° pitch angles, recommended for nominal endurance. Consequently, these positions were fixed and the servo control deactivated to avoid the noise that can be induced in the turbulence measurements from small shifts in battery position. To sample more frequently in the deep overflow plume, a typical flight pattern included a full dive followed by a climb to a turn depth of 450 m, followed by a dive and full climb (see Fig. 3a for a time series of pressure record). We shall refer to the full water column dives and climbs as ''full profiles,'' and the near-bottom climb–dive cycles with the turn depth of 450 m as ''half profiles.'' The maximum dive depth was set to 900- or 50-m height above the bottom detected by the altimeter. Both the glider and the MR recorded continuously. In total, 93 dive-and-climb pairs (i.e., 186 profiles) were made; 17 cycles toward the end of the mission were shallow dives, to about 100 m, to cope with encountered navigation problems. The remaining 76 dive-and-climb pairs are used in this paper, 36 of which were within the area identified in Fig. 2d, approximately collocated with the VMP stations. Of the 76 dive-and-climb pairs, 31 were half profiles. Typical flight properties of the glider, averaged over the entire mission and separated into full and half profiles of dives and climbs, are summarized in Table 1; see also section 5a. The asymmetry in the path angle and vertical velocity is not because of the MR but because of overriding the servo control using fixed battery positions.

4. Data processing

a. Glider

The glider data are processed using the software kindly provided by Dr. Gerd Krahmann (GEOMAR, Germany). After converting the data to physical units, a best guess of the glider's position is made based on the GPS fixes and the glider's internal navigational calculations. The top and bottom turns are identified from pressure, and the time series are separated into dive-and-climb profiles. The CTD pressure sensor is found to be more accurate than the navigation P sensor and in good agreement with the MR P sensor, and is used throughout. Time series of all variables from the glider are interpolated to a common time at 1-s intervals.

The angle relative to the horizontal that the glider ascends or descends is the glide angle,

$$\gamma = \theta + \mathrm{sgn}(\alpha), \tag{1}$$

where θ is the pitch angle and α is the angle of attack (AOA); see Fig. 1 for an illustration. The pitch and roll are measured by the glider's navigation sensor and, more accurately, by the inclinometer on the MR. The glider speed through water, U, and AOA are crucial parameters that must be estimated as accurately as possible for high-quality dissipation rate measurements (section 4b). Here we use a hydrodynamic flight model summarized in Merckelbach et al. (2010) to obtain U and AOA by optimizing three calibration parameters: the drag coefficient, glider volume, and hull compressibility.

In quasi-steady flight, the balance of horizontal and vertical forces acting on the glider can be written as

$$F_B - F_g - \frac{\rho S_w U^2}{2}(C_{D_0} + C_{D_1}\alpha^2)\frac{\sin^2\gamma + \cos^2\gamma}{\sin\gamma} = 0. \tag{2}$$

This is Eq. (13) of Merckelbach et al. (2010) after correcting for a sign error in the last term. In the flight model formulations, we retain the convention of positive path and pitch angles when the glider points up, to be consistent with Merckelbach et al. (2010), which is also in accordance with the convention used by the Slocum; however, we use the right-handed convention when presenting the data. In Eq. (2), C_{D_0} and C_{D_1} are the

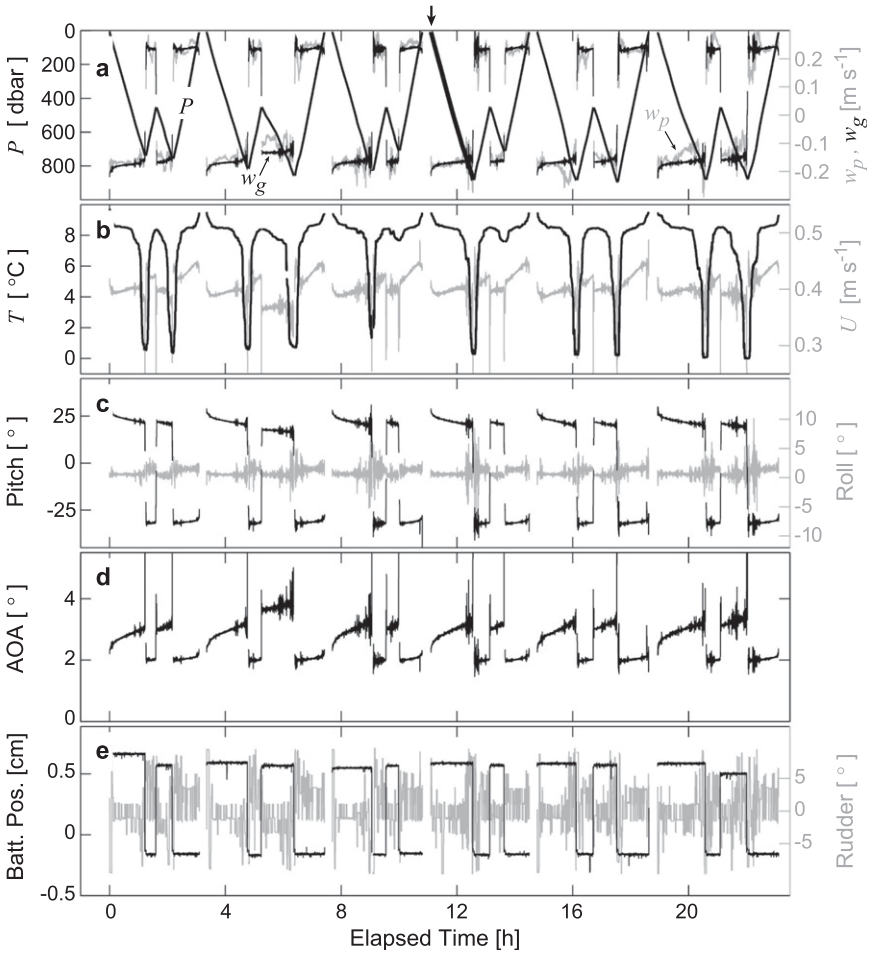

FIG. 3. Flight behavior data from an arbitrary sequence of dives and climbs. Time is referenced to the start of the first dive at 0040 UTC 6 Jun 2012. Time series of (a) P and w_p (gray) inferred from the rate of change of P and w_g (black) from the flight model, (b) T and U (gray), (c) pitch and roll (gray), (d) AOA, (e) central battery position, and rudder angle on the tail fin (gray). Data in (a)–(d) are measured by the MR, decimated to 4 Hz for the display, and (e) are measured by the glider. The P record shows the typical pattern with full dive and climbs interrupted by ''half'' climbs and dives with a turn depth at 450 m. The arrow and the thick portion of the profile in (a) mark the dive used in Fig. 4.

coefficients determining the total (i.e., sum of drag from both the hull and the wings) parasite drag and induced drag, respectively. The quantity S_w is the wing surface area; U is the glider velocity through water along the glider path; and $F_g = m_g g$ is the force due to gravity, where m_g is the mass of the glider and g is the acceleration due to gravity. The net buoyancy force F_B is defined as

$$F_B = g\rho\{V_g[1 - cP + \alpha_T(T - T_0)] + \Delta V_{\text{bp}}\}, \quad (3)$$

where ρ is the in situ density, V_g is the glider volume at atmospheric pressure, c is the compressibility of the hull, P is the water pressure, α_T is the coefficient of thermal expansion, T is the water temperature, T_0 is a reference temperature, and ΔV_{bp} is the buoyancy change resulting from the buoyancy engine of the glider. The AOA is obtained numerically from the expression

TABLE 1. Flight statistics for dives and climbs for the entire mission. Half dives and climbs refer to profiles with a turn depth of 450 m. Statistics are the mean and ±1 standard deviation.

Type	AOA (°)	Path angle (°)	w_g (cm s^{-1})	U (cm s^{-1})
Dive, full	2.9 ± 0.4	25.7 ± 1.6	−17 ± 1	39 ± 1
Dive, half	3.6 ± 0.6	22.0 ± 2.7	−14 ± 2	37 ± 3
Climb, full	2.0 ± 0.1	−33.4 ± 0.8	24 ± 1	43 ± 1
Climb, half	2.0 ± 0.1	−33.9 ± 1.1	24 ± 1	43 ± 2

$$\alpha = \frac{C_{D_0} + C_{D_1}\alpha^2}{(a_w + a_h)\tan(\theta + \alpha)}, \quad (4)$$

where a_h and a_w are the lift–slope coefficients for the hull and wings, respectively. The reader is referred to Merckelbach et al. (2010) for further details of the flight model. We calibrate the parameters C_{D_0}, c, and V_g by minimizing a cost function relative to the vertical velocity inferred from the rate of change of pressure w_p using a nonlinear least squares method. For the other parameters, we use the optimized values of $C_{D_1} = 2.88$, $a_w = 3.7\,\mathrm{rad}^{-1}$, and $a_h = 2.4\,\mathrm{rad}^{-1}$ reported in Merckelbach et al. (2010); $S_w = 0.1\,\mathrm{m}^2$; $m_g \sim 56.41\,\mathrm{kg}$; and use T, ρ, P, θ, and ΔV_{bp} as measured by the glider. Optimization is carried out in 1-day-long sets of full dives and climbs, separately, resulting in 14 estimates for each parameter. As expected, compressibility, c, and glider volume, V_g, did not show any discernible difference between dives and climbs (not shown). The drag coefficient, C_{D_0}, for dives were approximately 15% larger than the climbs on average, with no trend in the short deployment period. The average values (±1 standard deviation) using all data points are $C_{D_0} = 0.14(\pm 0.02)$, $c = 6.1(\pm 0.2) \times 10^{-10}\,\mathrm{Pa}^{-1}$, and $V_g = 55(\pm 0.1) \times 10^{-3}\,\mathrm{m}^3$. In the following we use the average values when applying the flight model to infer speed through water U and the vertical glider speed,

$$w_g = U\sin(\theta + \alpha). \quad (5)$$

For a regular deep Slocum without an MR, Merckelbach et al. (2010) obtained similar glider volume and compressibility values but C_{D_0} increased in time from about 0.09 to 0.12 through their 3-month deployment, presumably as a result of biofouling. The relatively large value of the drag coefficient obtained here, $C_{D_0} = 0.14$, is consistent with a deep Slocum glider equipped with an MR, giving a frontal area approximately 30% larger than a regular glider.

b. MR

Before converting the raw data from the MR into physical units, the pressure and thermistor channels recording the signal plus signal derivative are deconvolved to obtain high-resolution P and T records (Mudge and Lueck 1994). The MR time stamp P and T are then corrected against the glider data. An estimate of the vertical velocity is inferred from the rate of change of the high-resolution pressure record w_p and smoothed using a second-order Butterworth low-pass filter with a cutoff frequency of 0.2 Hz. Inclinometer data are low-pass filtered using the same filter. The AOA is inferred from the filtered pitch time series using Eq. (4). The glider along-path velocity (relative motion between the glider and the water) U and the vertical velocity of the glider are obtained from Eqs. (2) and (5), respectively. Time series of P, w_g, w_p, U, α, γ, and θ are then interpolated to the fast channel sampling rate of 512 Hz.

The shear probe voltage output is converted to shear using the known electronic constants, the sensitivity of the shear probe, and the flow past the sensors (see, e.g., Lueck et al. 2002). The time derivatives are converted to spatial derivatives along the main axis of the instrument (along x'), approximately equal to the along-path direction for small AOA. The shear (along x') is proportional to the raw output times the speed squared, and we use U that is inferred from the flight model.

The time series recorded by the MR are split into dive and climb profile segments. A profile segment is detected, below 5-m depth, when the glider ascended or descended with $|w_g| > 4\,\mathrm{cm\,s}^{-1}$, for a duration of at least 60 s. The small values of w_g are normally associated with maneuvers at the turn points from climb to dive near the surface (or a predefined deeper level) or from dive to climb near the end of a dive. At these turn points, the AOA is large and flow past the sensors is nearly zero; therefore, the shear probe data cannot be used. A deep glider maneuvers slowly before it achieves a nominal glide angle; hence, we excluded 20 s of the record at each end of the detected profile segment. Occasionally, segments with $|w_g| < 4\,\mathrm{cm\,s}^{-1}$ can be observed in a dive or climb profile, particularly at the interfacial layer with large shear. A dive or climb profile may thus consist of several subsets (detected using the same algorithm), each of which are processed separately to measure ε, and then merged together into a single dive or climb profile.

The time series of shear is used to calculate ε. The record from each shear probe is segmented into half-overlapping 12-s-long portions for spectral analysis. A fast Fourier transform (FFT) length corresponding to 4 s is chosen, and each 4-s segment is detrended and Hanning windowed before calculating the spectra. The shear probe signal coherent with the accelerometer data (from the two-axis vibration sensor) is removed using the method outlined in Goodman et al. (2006). The removal of this signal is probably not necessary because the gliders are ballasted very close to seawater density (see discussion in section 5d). We calculate the dissipation rate using both the cleaned and the original shear spectra for further inspection. The Goodman method is based on the cross spectra between the shear probe and the accelerometer, and for best results and statistical significance, a record length several times greater than the FFT length is advised. We use 12-s segments, that is, 3 times the FFT length. The vibration sensor is not

TABLE 2. Statistics related to the dissipation rate calculations. Statistics are the 2.5, 50, and 97.5 percentiles, mean, and the maximum likelihood estimator (mle) of the mean from a lognormal distribution. Here, k_l and k_u are the lower and upper wavenumber integration limits, corr is the correction for the unresolved variance, u_t is the turbulent velocity scale, R is the ratio of speed through water and u_t, and ε_d is the "dirty" estimate of ε before removing the signal correlated with the accelerometer.

	2.5%	50%	97.5%	Mean	mle
k_l (cpm)	0.6	0.6	0.7	0.6	—
k_u (cpm)	2.5	10.9	40.5	15.6	—
corr (−)	1.6	1.8	2.9	2.0	—
u_t (cm s^{-1})	0.01	0.1	1.7	0.3	0.3
R (−)	24	280	2995	591	638
ε_d (W kg^{-1})	4.0×10^{-11}	5.9×10^{-9}	8.6×10^{-7}	9.7×10^{-8}	2.0×10^{-7}
ε (W kg^{-1})	3.0×10^{-11}	3.7×10^{-9}	5.7×10^{-7}	6.3×10^{-8}	1.4×10^{-7}
$\varepsilon_d/\varepsilon$ (−)	0.9	1.6	4.2	1.8	1.8

calibrated because a signal in physical units is not required for the Goodman algorithm.

The frequency domain shear spectra $\Phi(f)$ are converted into along-path wavenumber k domain using Taylor's frozen turbulence hypothesis and the glider speed, as $\Phi(k) = U\Phi(f)$ and $k = f/U$. For a typical $U \sim 0.4\,\mathrm{m\,s^{-1}}$, the FFT length is equivalent to 1.6-m along-path length and resolves the low wavenumber part of the spectrum that is crucial for the roll off for low dissipation rates. The wavenumber spectra are then corrected for the shear probe's limited spatial response with a cutoff wavenumber of $k_c = 48$ cpm, by dividing $\Phi(k)$ by the transfer function $H(k) = 1/[1 + (k/kc)^2]$ (Macoun and Lueck 2004). The dissipation rate of TKE for each segment is calculated, assuming isotropic turbulence, by integrating the wavenumber spectrum as

$$\varepsilon_j = \frac{15}{2}\nu\overline{\left(\frac{\partial u_j}{\partial x}\right)^2} = \frac{15}{2}\nu\int_{k_l}^{k_u}\Phi(k)\,dk, \qquad (6)$$

where $j(=1, 2)$ identifies the shear probe number ($u_1 = w$ and $u_2 = v$), ν is the kinematic viscosity that is a function of the local water temperature, and the overbar denotes averaging. The empirical model for the turbulence spectrum determined by Nasmyth (1970) is used to set the lower (k_l) and upper (k_u) integration limits of the spectrum and to correct for the variance in the unresolved portions of the spectrum. We use the accurate curve fit for the Nasmyth spectrum given in Wolk et al. (2002). The Nasmyth form indicates that 90% of the variance is resolved by integrating to $0.5k_K$, where $k_K = (2\pi)^{-1}(\varepsilon/\nu^3)^{1/4}$ is the Kolmogorov wavenumber [in cycles per meter (cpm)]. An initial estimate of ε is made by integrating in the normalized wavenumber range $0.015 < k/k_K < 0.05$, and then iteratively adjusting the integration band (widening for large ε, or narrowing for small ε, but keeping k_l greater than 1 cpm and k_u less than 40 cpm). Finally, the dissipation rate in the segment is calculated as the average of the values from both probes if they agree to within a factor of 4, or the minimum of the two otherwise (spikes can occur because of, e.g., hitting plankton). For each segment, two average values of ε are obtained: one before and one after cleaning the shear spectrum using the Goodman method. Statistics of integration band limits, correction factor for the unresolved variance, and original and cleaned dissipation rates are given in Table 2. The average correction for the unresolved variance of shear, using the Nasmyth's form, is a factor of 2. On average, the removal of the shear variance correlated with the accelerometer signal results in a reduction in dissipation measurements by a factor of 1.8.

c. VMP

The processing of the shear probe data from the microstructure profiler, VMP, follows established methods, and is similar to the processing of the MR data. The profiles of ε were calculated using the isotropic relation [Eq. (6)], but for the vertical wavenumber k_z spectrum and using the shear components $\partial u/\partial z$ and $\partial v/\partial z$. The VMP is stable in the water column as a result of its mass, and sinks typically to within a few degrees from the vertical, at an approximately constant speed of $0.6\,\mathrm{m\,s^{-1}}$. Average (plus or minus one standard deviation) sink velocity over all profiles was 0.61 ($\pm$0.03) m s^{-1}, and the assumed frozen turbulence hypothesis typically holds (mean flow past the sensors is larger than the velocity scale of the turbulent eddies). The VMP is equipped with a three-axis accelerometer vibration sensor, and all three components are utilized to obtain clean shear spectra (Goodman et al. 2006). The correction for the shear probe response, selection of the integration band, correction for the unresolved variance, and averaging over the two probes are as described for the MR (section 4b). Profiles of ε are obtained from the shear spectra using half-overlapping 6-s segments, using an FFT length of 2 s (corresponding to about 1.2 m), and produced as 2-m vertical averages to a noise level of $10^{-10}\,\mathrm{W\,kg^{-1}}$.

5. Results and discussion

a. Flight behavior

Time series of flight behavior data for a subset of the mission are shown in Fig. 3. The dive–climb cycles illustrate the pattern that samples the deep overflow water more frequently than the ambient. The data presented are representative of the entire mission. The fixed position of the center battery, nominally at 0.56 cm during dives and at −0.085 cm during climbs, led to an asymmetry with steeper ascents: pitch angles were approximately 22° and −32° during dives and climbs, respectively. The AOA was variable but typically small, always less than 4°, except near the turning points.

The water associated with the FBC overflow, typically colder than 3°C, and the stratified interface between the plume and the ambient, typically between 3°–6°C, can be seen in the deep portions of the profiles. All casts in Fig. 3, except the profiles near elapsed time 10 and 13 h with relatively shallow dives, sampled the plume and the interfacial layer. Near the interface and into the plume, the pitch and roll variance substantially increased. The AOA was smaller for climbs than for dives (2° ± 0.5° versus 3° ± 0.5°), and the AOA of the half dives following the turns at 450 m was typically 0.5° larger. The flight properties are representative of the entire mission; see the statistics for the entire dataset (76 dive–climb cycles), split into dives and climbs, and full and half profiles in Table 1. The average along-path glider speed was approximately constant ($U \sim 0.4\,\mathrm{m\,s^{-1}}$ to within 10%), independent of the type of the profile. Because of the larger pitch angle in climbs, the glider attained larger vertical velocities of about $0.24\,\mathrm{m\,s^{-1}}$. The flight properties are almost identical for full and half climbs. For the dives, however, the half profiles have approximately 20% smaller w_g and path angle, and about 0.7° larger AOA, with larger variability (standard deviation is 50% larger than the full dives).

The deepest dive, marked in Fig. 3a, is presented as a pseudovertical profile in Fig. 4, that is, the sampling along the slanted path is presented as profiles with respect to pressure. The increased variability in w_g and U, and the elevated variance in pitch, roll, and AOA can be observed as the glider penetrates the turbulent plume. An estimate of the vertical velocity of water is $w_p - w_g$. The profiles shown in Fig. 4a suggest low vertical wavenumber variability in the ambient, presumably associated with internal waves, and high wavenumber variability in the IL, due to entrainment and turbulent mixing.

While w_g is obtained from the flight model, a simple bandpass filtering of the w_p time series can achieve a comparable profile. Near the Luzon Strait, Rudnick et al. (2013) obtained vertical velocity profiles using filtering that compared very well to those obtained from a hydrodynamic flight model. In our dataset, representative bandpass limits correspond to time scales of approximately 10 and 100 s, obtained from comparisons of frequency spectra of w_g and w_p.

b. Microstructure data

Also presented in Fig. 4 are the temperature gradient and shear measured by the thermistors and the shear probes, all showing consistently quiescent portions in the interior, and patches of water with elevated turbulence, particularly in the bottom 150 m but also in the upper 200 m, and between 550 and 700 m. The profile is an arbitrary deep dive, representative of the other profiles covering the overflow plume. The independent measurements of temperature gradient and shear agree in patterns, lending confidence in the quality of the microstructure data. The high-resolution temperature profile shows numerous inversions indicative of turbulent overturns in the turbulent patches (Fig. 5), consistent with the elevated vertical velocity variance at the interface (Fig. 4a).

Indirect estimates of the dissipation rate, using the proportionality of the Thorpe overturn scale and the Ozmidov scale [Eq. (7)], are often made making use of temperature, or when possible density, measurements. Our calculations and analysis using the overturns are too lengthy to report in the present paper and are the topic for a future study. Overall, dissipation rates inferred from the Thorpe scale analysis compare favorably with the shear probe measurements reported here. Detailed analysis is needed; however, our data suggest that the gliders without turbulence probes can be used to infer mixing in turbulent waters. The glider's slanted path can lead to errors in the measurements of overturns (Thorpe 2012; Smyth and Thorpe 2012). Thorpe (2012) concludes that the error (an underestimate) of dissipation rate associated with Kelvin–Helmholtz (KH) billows is likely to be less than a factor of 2, and is greatest when the billow aspect ratio is greatest and the glider inclination angle is small. Transects at small inclination angles can lead to detection of false overturns when gliding through internal waves, and can give misleading estimates of the scale of overturns. The direct numerical simulations (Smyth and Thorpe 2012) suggest that the associated bias could be reduced by profiling in the cross-stream direction, and that uncertainties due to horizontal intermittency can be reduced by averaging over ensembles on the order of 100.

A pair of 50-m vertical segments centered at 345 and 775 m is extracted to present frequency and wavenumber spectra representative of the average spectra in turbulent and quiescent portions of the water column (Fig. 5).

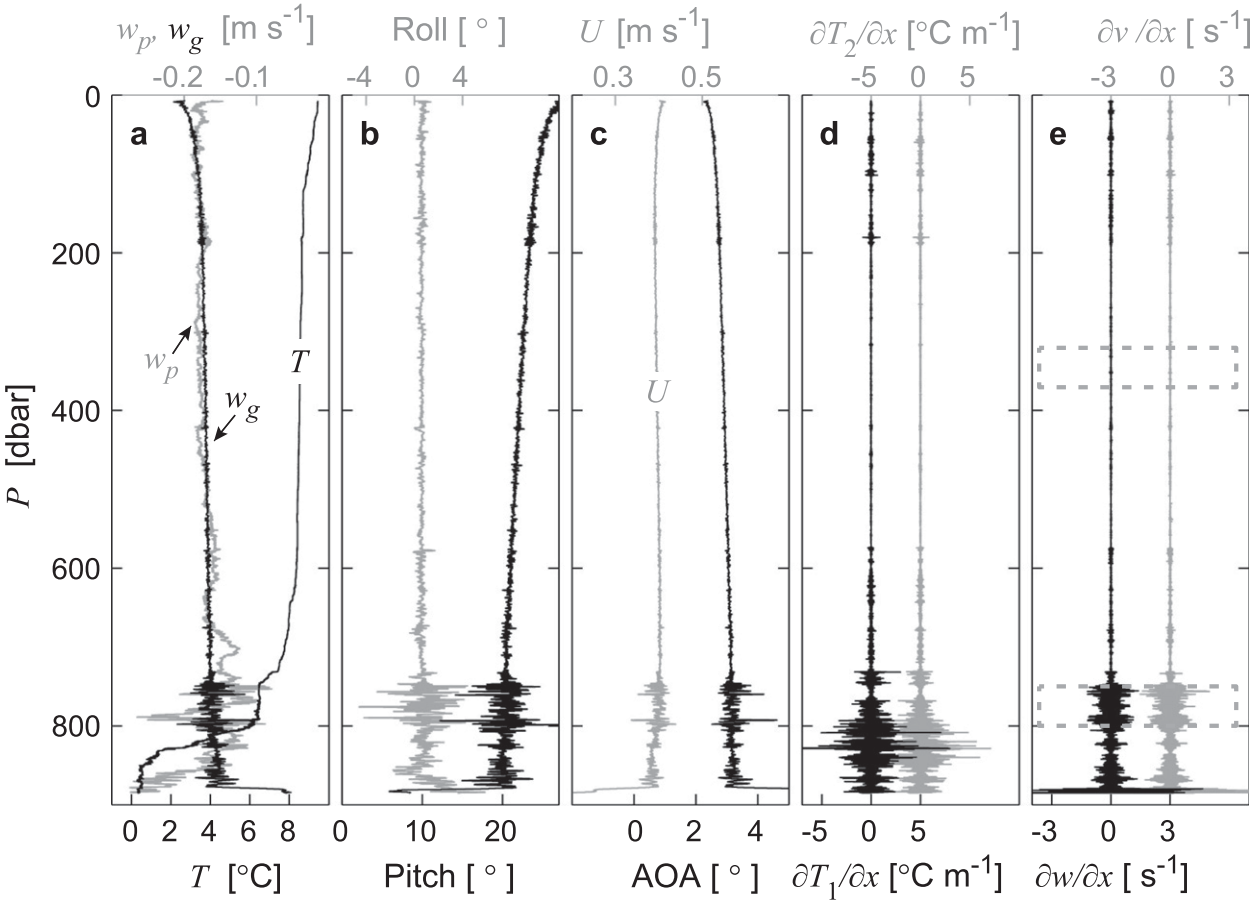

FIG. 4. Vertical profiles measured during the dive marked in Fig. 3a. Note that the sampling along the slanted path is displayed as profiles as a function of pressure. (a) Temperature T, pressure-derived vertical velocity w_p (gray), and vertical glider speed w_g (black); (b) pitch and roll (gray); (c) AOA and U (gray); (d) temperature gradients from the two thermistors; and (e) shear measured by the two probes. Dashed lines in (e) delineate 50-m-long (vertical) segments for which the quiescent and energetic spectra of Fig. 5 are shown.

The upper segment is from the relatively quiescent ambient, and the deeper segment is from the turbulent IL. In contrast to the quiescent segment with quasi-homogeneous temperature profile, the energetic turbulence in the IL is manifest in the temperature profile. The vertical extent of these segments is marked in Fig. 4e for reference. The 50-m vertical scale is approximately 25 times the typical 2-m vertical stretch of data (12 s) over which the dissipation profiles are calculated. Example spectra using 12-s segments from the same record, centered at 345 and 775 m, are shown in Fig. 6 to demonstrate the quality of the shear probe data. These examples are arbitrary and do not represent particularly good-quality segments.

The shear spectra are noisy at high frequency and wavenumber. From test dives of a shallow Slocum glider equipped with a MR, Wolk et al. (2009) discussed various vibrations at discrete frequencies. In the bulk of the profile, after the turning points are removed, the main source of vibration is the action of the glider's rudder, which controls the heading of the glider. The influence of the rudder on shear probe measurements is presented in detail in the appendix. Spectral analysis of segments of data subsampled when the rudder was in action shows peaks at high frequencies; however, this noise does not influence the quality of the shear probe measurements in the wavenumber and frequency bands of interest.

It is typical in ocean microstructure measurements that the shear spectra from short segments deviate from the empirical curve of Nasmyth, but approach it when averaged over relatively larger segments that are homogenous in turbulence intensity. The wavenumber spectra of shear presented in both Fig. 5 (50-m segment) and Fig. 6 (approximately 2-m segment) adhere to the Nasmyth's form. The empirical form for the quiescent segment is for $\varepsilon = 9 \times 10^{-10}\,\mathrm{W\,kg^{-1}}$ for the 50-m segment and for $\varepsilon = 3 \times 10^{-10}\,\mathrm{W\,kg^{-1}}$ for the 2-m segment, which are well captured to a wavenumber of 10 cpm,

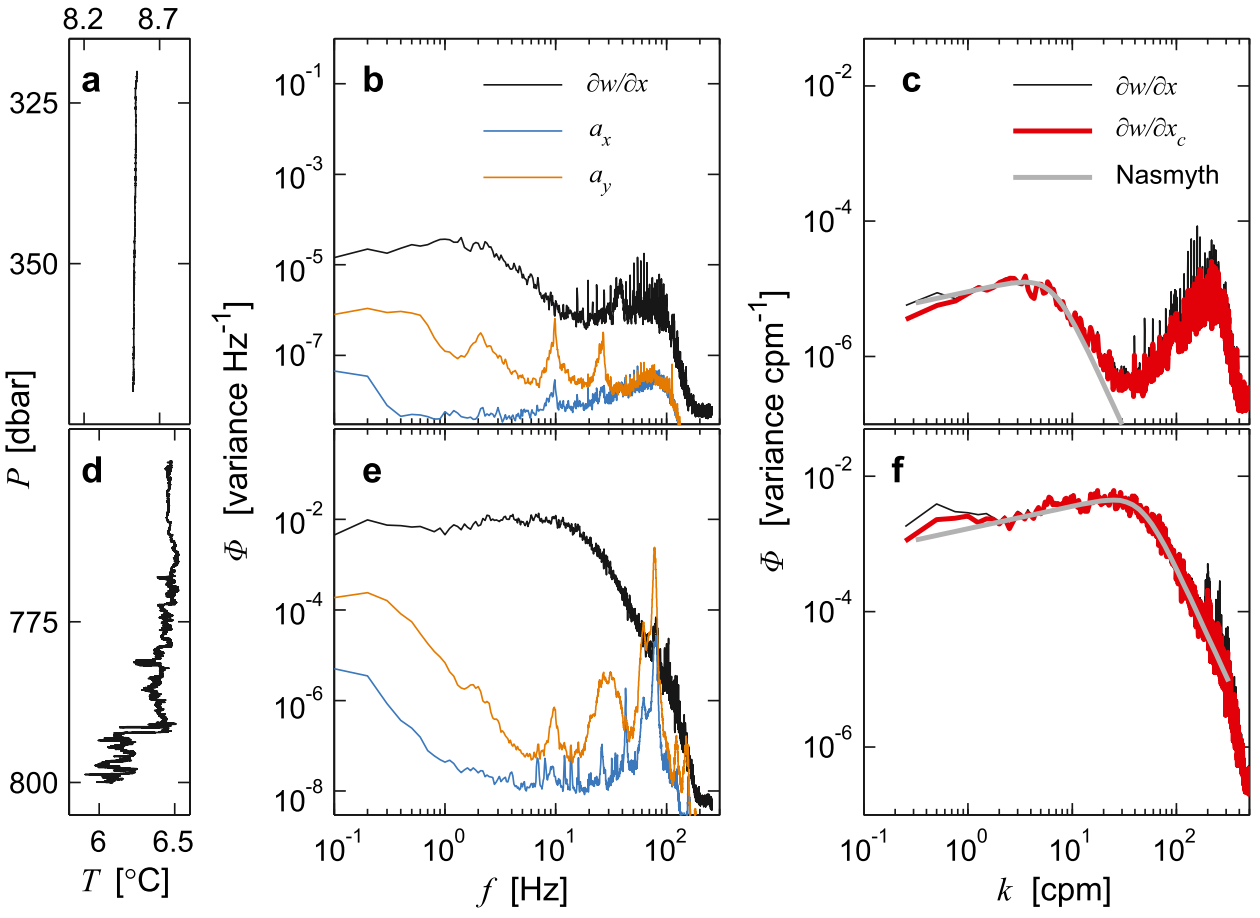

FIG. 5. Temperature profiles and various spectra calculated for the two 50-m-long segments identified in Fig. 4. (top) Quiescent segment. (bottom) Turbulent segment. (a),(d) Temperature profiles from thermistor 1; (b),(e) frequency spectra of acceleration measured by the two-axis vibration sensor (arbitrary units) and of shear from probe 1; and (c),(f) slant wavenumber spectra for the original (black) and cleaned (red) shear, and Nasmyth's dissipation spectrum (gray). The FFT length is 10 s. The dissipation spectra are plotted for 9×10^{-10} and 3×10^{-6} W kg^{-1} for the segments centered at 345 and 775 m, respectively. Flight information (angles in ° and velocity in cm s^{-1}): quiescent segment, $\theta = 20 \pm 0.2$, $\phi = 0.6 \pm 0.1$, AOA $= 2.9 \pm 0.02$, $w_g = -17 \pm 0.1$, $U = 40 \pm 0.1$; turbulent segment, $\theta = 18 \pm 2.1$, $\phi = 1.0 \pm 1.5$, AOA $= 3.2 \pm 0.3$, $w_g = -16 \pm 1.4$, $U = 40 \pm 1.3$.

suggesting that the noise level of the instrument is better. The shear spectra obtained from the glider are comparable to the high-quality spectra obtained from vertical microstructure profilers.

c. *Data selection*

In this subsection we discuss the influence of flow distortion, applicability of Taylor's frozen turbulence hypothesis, and summarize our criteria for selection of data segments for dissipation rate calculations.

Any in situ measurement of the velocity field will suffer from flow distortion near the sensors and the platform. Wyngaard et al. (1985) studied the possible errors in velocity covariances measured ahead of axisymmetric bodies. They found that for an ellipsoid of revolution with an aspect ratio L/D of 5:1, where L is the length and D is the diameter, measurements at a plane 0.5 D ahead of the body, along the axis, led to fractional errors on the order of 10% with weak dependence on the small AOA. Errors in variances generally decreased with distance from the axis of symmetry (note that the MR is placed off axis to the glider). Osborn and Lueck (1985) discussed the flow distortion effect on a 51-m-long research submarine with an aspect ratio of approximately 9:1. Their instruments were mounted 0.88D above the submarine hull (off axis). Potential flow calculations indicated that at nil AOA, the reduction in the mean flow past sensor was 5% at the level of the probes, with a 9% decrease in the variance of $\partial w/\partial x$ and an 11% increase in the variance of $\partial v/\partial x$. Note that the opposing effect on the variance of orthogonal components of shear approximately average out. Our measurements on the glider with an aspect ratio of 8:1, at a plane 0.77D ahead of the glider nose, and 0.72D off the glider axis,

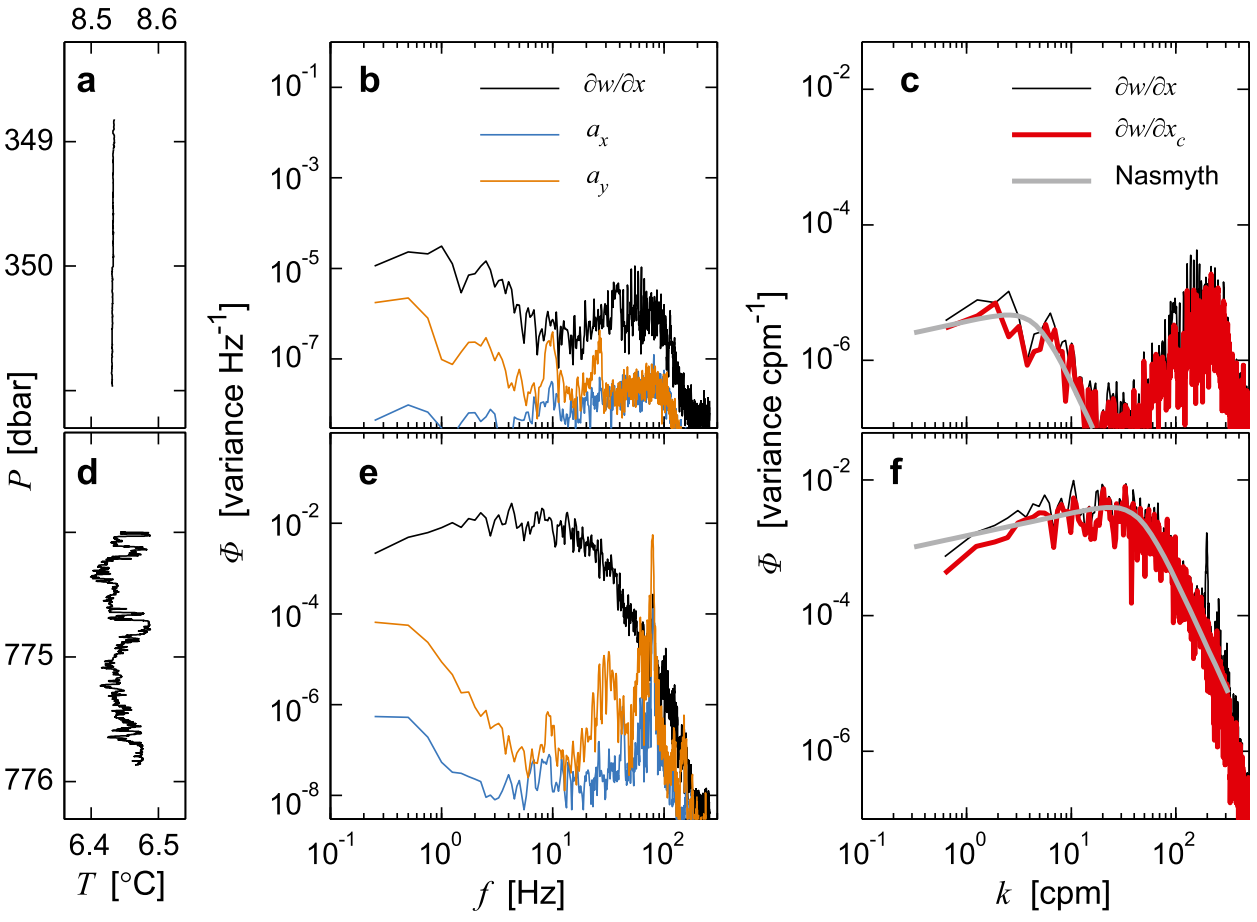

FIG. 6. As in Fig. 5, but using 12-s-long data centered at 350 m in the quiescent segment and at 775 m in the turbulent segment. The FFT length is 4 s. The segment length and the FFT length are identical to those used in calculating profiles of ε. The vertical stretch of the record is 2.2 and 1.9 m, respectively, for the quiescent and turbulent segments. The Nasmyth spectra are plotted for 3.2×10^{-10} and 2.6×10^{-6} W kg^{-1}. Flight information is identical (to within 1 standard deviation) to the values for Fig. 5.

above the glider hull, are comparable to the measurements of Osborn and Lueck (1985). Overall, we conclude that the effect of flow distortion is negligible compared to other error sources.

When the velocity scale of the largest eddies is comparable to the glider speed, the applicability of the Taylor's hypothesis for frozen turbulence is not valid. Furthermore, the glider flight behavior may be affected, leading to large AOA, and contamination of flow may occur due to recirculations from the wake of the instrument. In the following, we estimate a turbulent velocity scale, u_t, and use the ratio $R = U/u_t$ to detect and exclude the segments inconsistent with the assumptions of the Taylor's hypothesis.

A turbulent velocity scale can be inferred from the measured dissipation rate using $u_t \sim (\varepsilon l)^{1/3}$ and substituting for the turbulent length scale l the Ozmidov length, using

$$L_O = (\varepsilon/N^3)^{1/2}, \tag{7}$$

giving

$$u_t = (\varepsilon/N)^{1/2}. \tag{8}$$

The buoyancy frequency is

$$N(z) = [-(g/\rho_0)\partial\sigma_\theta/\partial z]^{1/2}, \tag{9}$$

where ρ_0 is a reference density and $\sigma_\theta(z)$ is the observed potential density anomaly profile. The MR does not measure the salinity and that measured by the glider CTD sensor (unpumped) needs corrections. Because the salinity–temperature relation in the Faroe Bank Channel is precise, and for simplicity, we infer density from the temperature profiles. All σ_θ and temperature profiles from the ship's CTD system are used to obtain a third-order polynomial fit of σ_θ against T. Prior to obtaining the fit, the data are averaged in 0.01 kg m^{-3} wide bins of σ_θ. The difference in the fitted and the

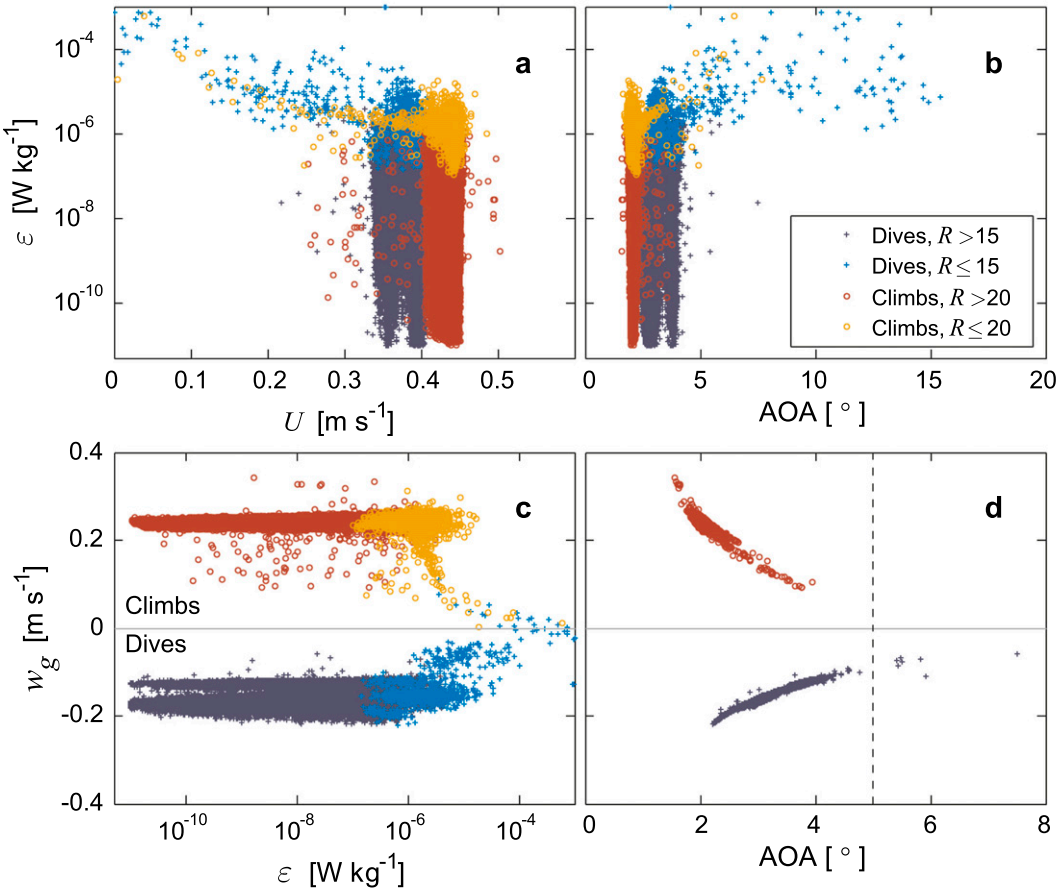

FIG. 7. Scatterplots of (a) U and (b) AOA against ε and (c) ε and (d) AOA against w_g for dives (blue crosses) and climbs (red circles). Paler colors mark the segments when Taylor's hypothesis is suspect. In (d), only the segments with $R > 15$ (dives) and $R > 20$ (climbs) are shown, and the dashed vertical line marks AOA = 5°.

original density profile varied to within ±0.06 with an rms error of 0.015 kg m^{-3}. The buoyancy frequency calculated from 1-m average values using centered differencing of sorted σ_θ profiles measured by the CTD and inferred from T agreed to within an average fractional error of 40%. In calculating N, the potential density is inferred from the T profile measured by the glider after averaging the T profile in 1-m vertical bins. The density profile is then sorted into a stable profile and interpolated to the glider depth. Using unsorted density profiles averaged in 5-m vertical bins gives similar results.

For each segment where ε is available, the ratio $R = U/u_t$ and the average flight properties (U, w_g, γ, AOA) are calculated. Statistics of the inferred turbulent velocity scale u_t and the ratio R are given in Table 2. Scatter diagrams of chosen parameters are shown in Fig. 7. The data points with small values of R, when Taylor's hypothesis may fail, are highlighted with paler colors. When the glider speed relative to the water is not sufficiently stronger than u_t, the dissipation rate spuriously increases, with segments associated with large AOA and small w_g. Note that in Fig. 7d, the values with small R (threshold quantified below) that are associated with AOA exceeding 15° (see Fig. 7b) are excluded. Some dive segments with AOA > 5° exist even with $R > 15$.

A threshold for R to delineate high-quality data is estimated by inspecting AOA and the ratio of dissipation rate measured by the two shear probes, averaged in bins of R. In isotropic conditions and when the flow distortion is negligible, agreement is expected between the two shear probes mounted orthogonal to each other. All other factors set equal (uncertainties in viscosity, flow speed, assumption of isotropy, variance correction, etc.), the typical uncertainty associated with shear probe measurements and calibration errors is about 20% (see, e.g., Moum et al. 1995).

The ratio $\varepsilon_1/\varepsilon_2$ and the AOA averaged in unit bins of R are shown in Fig. 8 for relatively small R where the data quality starts degrading. For small values of R during dives, the MR is probably in the wake of the glider.

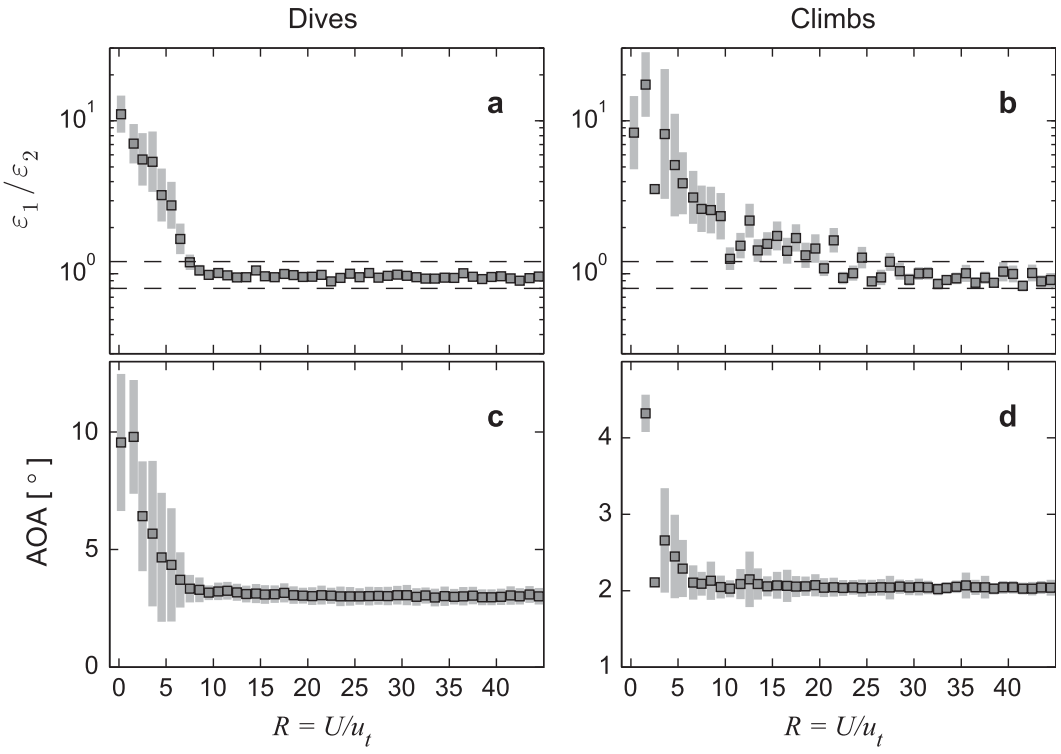

FIG. 8. Influence of R on (a),(b) dissipation measurements and (c),(d) AOA. Ratios of dissipation rate from shear probes 1(ε_1) and 2 (ε_2) and the AOA for (a),(c) dives and (b),(d) climbs, respectively. Only values for $R < 50$ are shown to emphasize the regime when the Taylor's hypothesis breaks down. Data are averaged in unit bins of R, and the gray shading indicates the 95% confidence intervals for the ratio $\varepsilon_1/\varepsilon_2$ and 1 standard deviation for AOA. Dashed lines in (a),(b) indicate ±20% agreement between the two shear probes.

Approximately 34% and 3% of R had values greater than 500 and less than 15, respectively (similar for both dives and climbs). Typically, there are 60–180 dive or climb data points in each bin for $R > 5$ and 10–50 data points for smaller values of R. The mean expected from a log-normal distribution is shown for $\varepsilon_1/\varepsilon_2$, together with the 95% confidence levels (Baker and Gibson 1987), whereas the average and one standard deviation are shown for AOA. The two probes typically agree to within 20% for large values of R, whereas there is significant deviation for $R \leq 15$ in dives and for $R \leq 20$ in climbs. The AOA also substantially increases when $R < 10$, more so for dives, and shear probe measurements are not reliable. Based on this analysis, we choose a threshold of $R = 15$ for dives and $R = 20$ for climbs. Setting the threshold to $R = 15$ for both dives and climbs does not change our results (survey-averaged profiles and probability distribution functions).

In summary, a segment satisfying any of the conditions—$R \leq 15$ for dives and $R \leq 20$ for climbs, AOA $\geq 5°$, $|w_g| < 0.04\,\mathrm{m\,s^{-1}}$, or $|w_g| > 0.5\,\mathrm{m\,s^{-1}}$—is flagged as bad. The total number of segments, climbs and dives combined, after data screening is about 67 700, shared as 61% dives and 39% climbs. The total number of removed points is about 3000—that is, about 4%—in approximately equal proportions from dives and climbs. Of the removed segments, about 85% are excluded because of the R criterion alone. For reference, the total number of 2-m averaged VMP data points is approximately 29 000.

d. Shear spectra

The shear spectra from the two example segments were shown in Figs. 5 and 6, demonstrating the high quality of the data and the ability of the glider to sample ocean microstructure. Here, we present shear spectra from the entire dataset, averaged in one decade bins of ε (Fig. 9). Thousands of spectra are averaged (except the largest ε bin with 895 segments), using only the good-quality segments (section 5c) but also including the shallow 100-m dive–climb cycles. The frequency spectra approach a common noise floor at high frequencies. The influence, on average, of cleaning the spectra with the Goodman et al. (2006) method can be seen by comparing the color curves with the gray curves in Fig. 9a. The most variance removed associated with the accelerations is at frequencies above 8 Hz. The largest corrections are in the

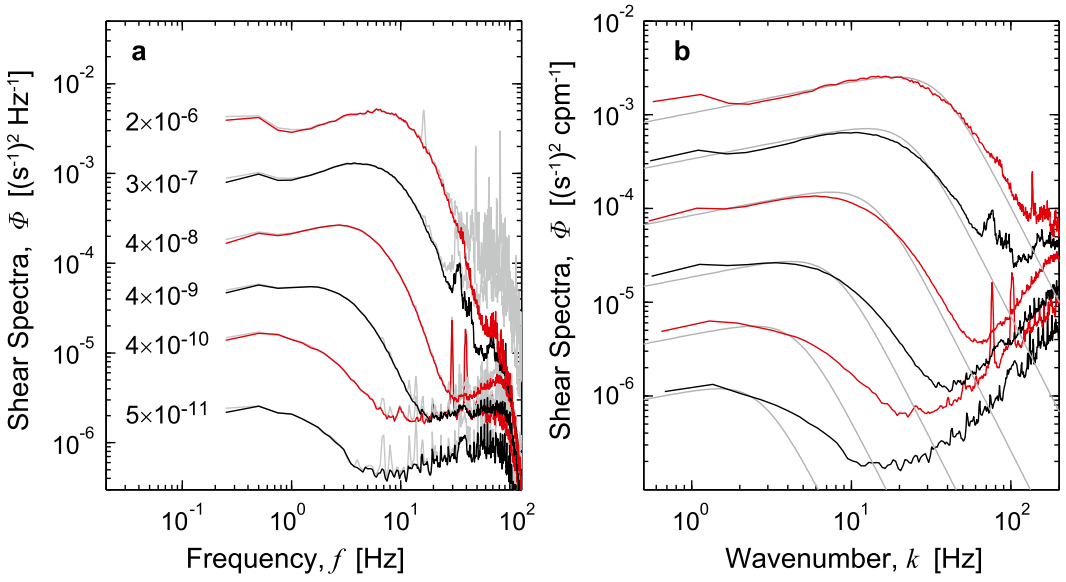

FIG. 9. Shear spectra averaged in bins of ε. Spectra are averaged in total from 6055, 16 452, 20 052, 17 379, 9058, and 895 segments within decadal bins between 10^{-11} and 10^{-5} W kg^{-1}. (a) Frequency spectra from shear probe 1. Alternating black and red curves are the clean shear spectra after removing the parts of the signal coherent with the accelerometers. The gray curves are the corresponding original shear spectra prior to cleaning. Average dissipation rate (W kg^{-1}) in each bin is indicated. (b) Wavenumber spectra averaged from both shear probes. Alternating black and red curves correspond to the dissipation rates indicated in (a). The gray curves are the Nasmyth spectra for the given ε values.

more energetic spectra, where the water is turbulent and the glider experiences substantial accelerations and rudder activity. The shear spectra are not contaminated in the frequency and wavenumber range used in the dissipation calculations. The cleaning of the shear spectra with the Goodman method removes variance from the low wavenumber of the spectra (see, e.g., Figs. 5 and 6). Because the glider is so light in the water, its movements at scales comparable to the glider size are likely related to turbulent eddies. The removal of this variance can lead to an underestimate of the actual turbulent dissipation rate. The comparison in Table 2 shows that dissipation measurements using the original spectra are, on average, 80% larger than those calculated using the cleaned spectra. The wavenumber spectra (Fig. 9b) broadly follow the Nasmyth's curve, evaluated for the average ε in each bin, at least to the wavenumber where the spectrum starts to roll off. Note that even the least energetic spectrum with $\varepsilon = 5 \times 10^{-11}$ W kg^{-1} has a marginally acceptable shape, suggesting a low noise floor for dissipation measurements using shear probes from a glider.

The average wavenumber shear spectra and the Nasmyth's dissipation spectrum differ (see, e.g., Fig. 9b), which is typical in ocean microstructure measurements. In the glider dataset, the peak at the dissipation spectrum is smoothed and the roll off is less steep compared to the Nasmyth's spectrum. There is variability in the speed used in calculating the wavenumber spectrum, before obtaining the average spectrum, that can smear out the spectral shape; however, this is not substantial (the variability is less than 5%). The imperfect agreement between the observed and the empirical spectra can partly be attributed to the intermittency (section 5f). Nasmyth (1970) observed, similar to our observations, a reduction in the curvature in the transition region between the inertial subrange and the dissipative subrange of measured spectra, and also that the spectra rolled off less steeply relative to the universal curve. He proposed the intermittency and the buoyancy effects (as the turbulence decays) to be the most likely factors to account for the observed spectral shapes. This is consistent with our dataset; also note that the spectra roll off more gently for low ε, which is typically associated with small turbulent activity index and fossil turbulence (section 5f). The agreement between the measured spectra and the empirical curve is better for the 50- and 2-m average spectra shown in Figs. 5 and 6, respectively. This is not in conflict with the role of intermittency in contributing to the discrepancy between the bin-averaged observed and empirical spectra. The 50- and 2-m spectra are from rather homogeneous (in turbulent intensity) patches of turbulence and are sampled in relatively short time, whereas the bin-averaged spectra cover a factor of 10 variability in ε and are sampled at different times and locations throughout the field work.

e. Comparison with VMP

A comparison between the glider-inferred dissipation rate and that measured by the vertical profiler VMP is attempted. Because of the inherent variability in the FBC, the intermittent nature of turbulence, and the separation between the ship and the glider, comparisons are only possible in the average sense, as for example, survey-averaged profiles (time and spatial averaging) and histograms or probability distribution functions (pdfs).

Survey-averaged profiles are compared in two sets, the entire survey and a subset of collocated profiles (Fig. 2d), and using different vertical coordinates. Because the turbulent overflow plume is bottom attached (Fer et al. 2010), and the thickness of the turbulent layer varies on the scale of 3–4 days (Seim and Fer 2011), we average with respect to 1) height above bottom; 2) the vertical distance from the 3°C isotherm, z_{3C}; and 3) isotherms. Similar averaging (1 and 2) was used in Fer et al. (2010) and Beaird et al. (2012). Method 1 successfully averages the turbulent bottom layer but smears out the structure in the layer above; method 2 concentrates in the thick and turbulent IL—the 3°C isotherm is a good proxy for the depth of the maximum stratification in IL; method 3 removes the influence of variability due to, for example, internal waves. Average profiles are shown in Fig. 10 for the VMP, for glider profiles separated into dives only, climbs only, and dives and climbs together.

There is no systematic difference between the average profiles inferred from dives and climbs, and the average of the two can be used to increase the statistical significance. The profiles of ε calculated from the VMP and the glider agree in the turbulent BL and in the isotherms colder than 5°C; however, they differ by up to one order of magnitude in the upper part of the IL (Fig. 10). When the survey-averaged profiles are calculated using full-depth dives and climbs only, the results in the IL are not improved (Fig. 10e). When the subset of glider and VMP data, which is collocated, is further restricted to the same period between 5 and 8 June, the profiles show the similar pattern but with a slightly larger variability (not shown).

The pdfs of dissipation rate measured by the VMP and the glider are presented in Fig. 11 for subsets of the data conditionally sampled in temperature, for waters below the 3°C isotherm, in the IL between 3° and 6°C, and higher above in the water column with T between 6° and 9°C. The upper temperature threshold is imposed to exclude the upper 50 m or so, to avoid the possible influence of different surface forcing. The pdfs are consistent with the results from the survey-averaged profiles. Dissipation measurements from both instruments in the cold layer show similar distributions but differ substantially in the warmer layers. Also shown in Fig. 11 are the lognormal pdf, fitted (using nonlinear least squares technique with the mean and standard deviation set as free parameters in the lognormal distribution) to the measured distribution curves using the bins between 10^{-9} and $10^{-6}\,\mathrm{W\,kg^{-1}}$. The bins are chosen to exclude any influence of the noise level of the instruments and contamination at large ε. The mean value from the fit and the maximum likelihood estimator (mle) from a lognormal distribution (i.e., using the measured data points, not the pdf curve) are summarized in Table 3. The average mle and that obtained from the lognormal fit in the restricted ε band are approximately the same for the VMP. On the other hand, for the glider, values obtained from the fit to the pdf curve are almost a factor of 2 larger than the mle values. This suggests substantial contribution to the glider data with $\varepsilon < 10^{-9}\,\mathrm{W\,kg^{-1}}$. The pdf obtained for temperatures above 6°C is broader for the glider data, with a relatively large contribution from the tails of the distribution, resulting in larger average values manifested in the profiles. The glider average values are approximately a factor of 3 and 9 times larger than the VMP values in the layers defined by the isotherms 3°–6° and 6°–9°C, respectively.

A similar analysis was conducted for the subsets of the data conditionally sampled for the turbulent activity index, $I_A = \varepsilon/\nu N^2$, for $I_A < 500$, $500 \le I_A < 5000$, and $5000 \le I_A$. The results are presented in Fig. 12 and Table 4. The analysis suggests that the main discrepancy between the VMP and glider ε values stems from sampling in the waters with less energetic turbulence with $I_A < 500$. For larger I_A, the pdfs are very similar; a two-sample χ^2 test for discrete data rejects the null hypothesis, at the 95% confidence level, that two samples come from the same distribution; that is, it suggests that the VMP and the glider data are drawn from the same population. The average values of ε are in excellent agreement for the most energetic turbulence, and they agree to within a factor of 2 for $500 \le I_A < 5000$ (Table 4).

The agreement between the VMP and glider-measured ε is excellent in the bottom 100 m and higher above the plume, when averaged with respect to height above bottom. When averaged in isothermal coordinates, the agreement is excellent up to the 5°C isotherm. There is, however, significant difference, reaching up to one order of magnitude, in the upper part of the IL and above, particularly between the 6° and 8°C isotherms. The pattern in the survey-averaged profiles that shows the largest discrepancy at 150–250 m above bottom (or 20–100 m above the depth of z_{3C}, or between the 6° and 8°C isotherms) is robust and not a result of the choice of

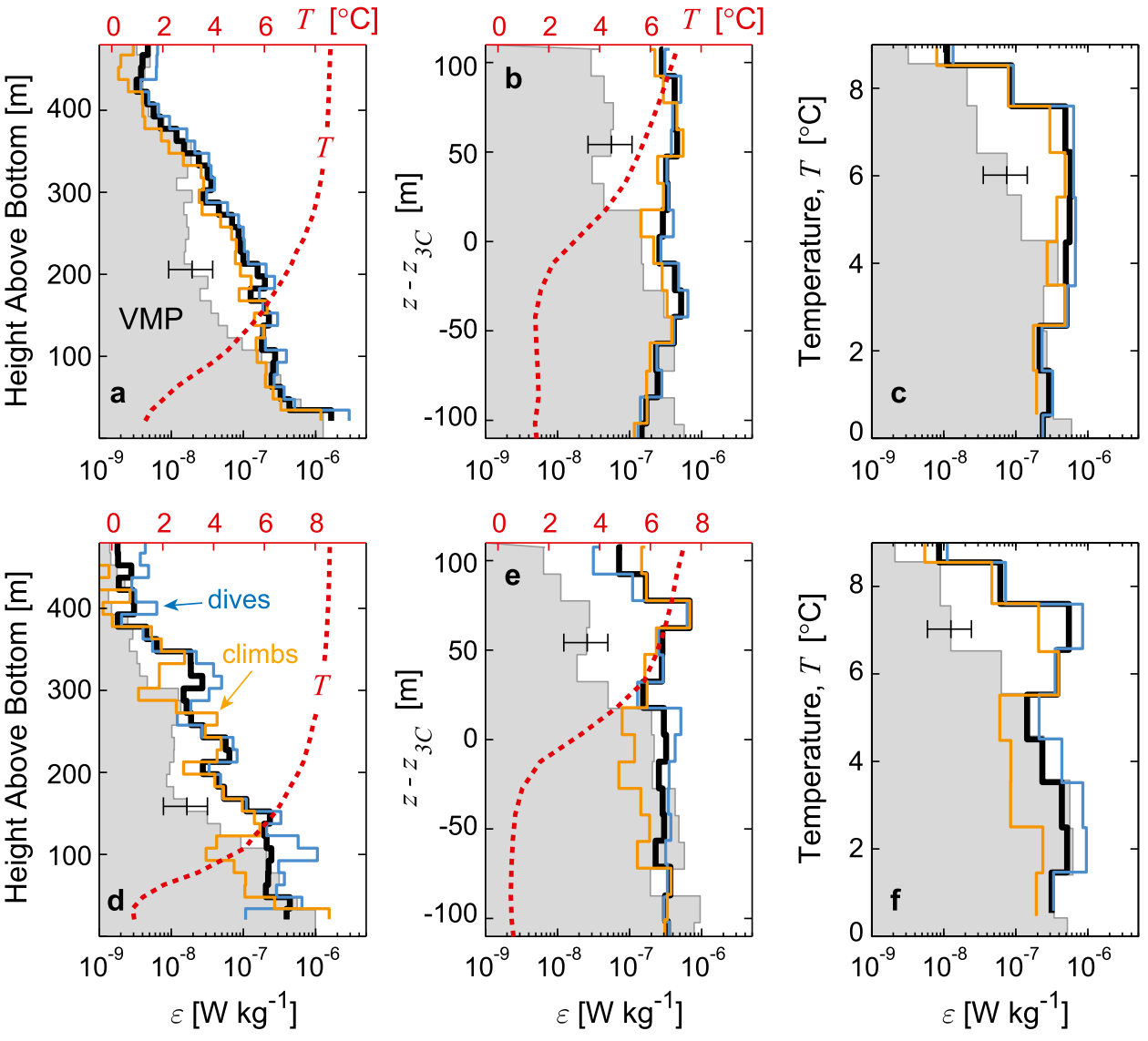

FIG. 10. (a),(d) Survey-averaged profiles of ε inferred from the VMP (gray) and the glider (dives only in blue; climbs only in orange; dives and climbs in thick black); and for reference, the average T profile (red dashed, upper axis) from the glider; the average T profile from the VMP is similar and not shown. (b),(e) As in (a),(d) but for ε vs $(z - z_{3C})$. (c),(f) As in (a),(d) but for ε vs T and without the red temperature plots. (top) Averages over all stations and dive–climbs. (bottom) Averages over the collocated stations and dive–climbs marked in Fig. 2d using the deep profiles only. Averaging is done (a),(d) with respect to height above seabed in 15-m-thick bins; (b),(e) relative to the depth of the 3°C isotherm in 15-m thick bins; and (c),(f) with respect to isotherms in 1°C bins. The horizontal error bars, placed arbitrarily, mark a factor of 2 in variability.

averaging in space or time, or using dives or climbs, or because of some outliers. Detailed analysis and inspection of the glider data suggest that the data are of high quality and the measured ε is reliable; we found no convincing evidence to discard the glider measurements where there is disagreement with the VMP data. The discrepancy most likely arises from 1) the different sampling—it is not clear that vertical, horizontal, or slanted transects should produce similar turbulence profiles; 2) intermittency of turbulence; and 3) the IL with enhanced stratification and shear. Points 1 and 2 are general, whereas point 3 is more site and instrument specific: in contrast to the vertical profiler, the glider penetrates the thick IL slowly and moves horizontally, sampling turbulent waters for a longer duration.

Previous studies that compared horizontal, sawtooth, and vertical transects of oceanic turbulence similarly showed large discrepancies between the different sampling transects. Yamazaki et al. (1990) compared turbulence measurements made from a submarine and a

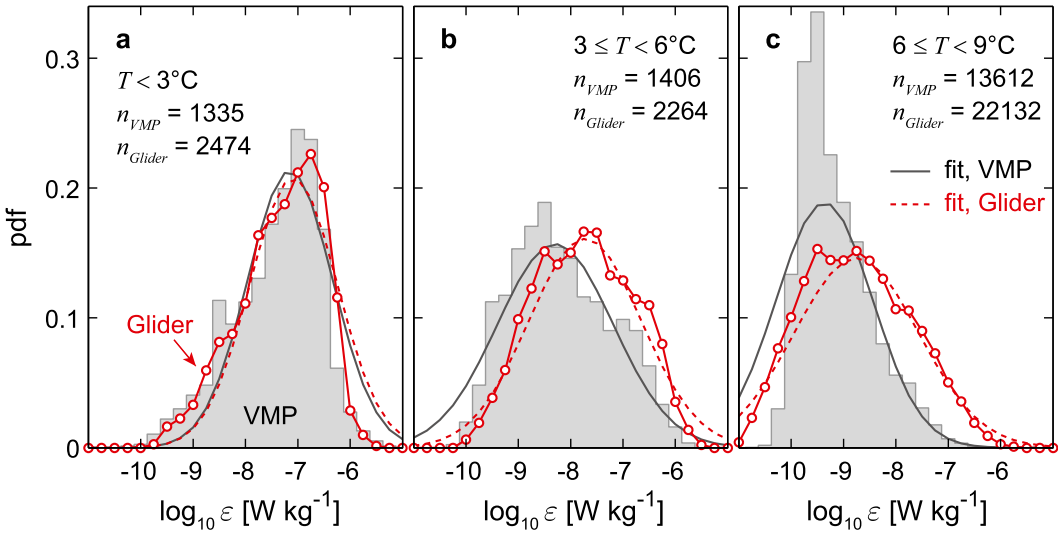

FIG. 11. Pdfs of ε, conditionally sampled from temperature classes (a) $T < 3$°C, (b) $3 \le T < 6$°C, and (c) $6 \le T < 9$°C, using the collocated VMP (gray shading) and the glider (red solid line) datasets. Smooth curves are lognormal distributions (VMP in gray; glider in red dashed) least squares curve fit to the pdfs in the range $10^{-9} \le \varepsilon \le 10^{-6}$ W kg^{-1}. Total number of data points in each dataset is indicated.

vertical profiler. The submarine cycled repeatedly between 50- and 120-m depths, with a path angle of approximately 6° (i.e., less than the glider's 20°–35°). They explained the difference, of approximately a factor of 2, between the average dissipation rates from the two systems by the bimodal distribution of turbulence (active and quiescent turbulence) and that the vertical profiler preferentially sampled the active distribution. We did not observe a bimodal distribution. Nasmyth (1970) reported results from measurements using a towed body equipped with microstructure sensors collecting data approximately at constant depth and in a cycling mode with ascent–descent angles of approximately 30°, comparable to the glider. Both measurements were centered at the same depth of about 210 m, away from the direct influence of surface forcing, at the same site, but at different times. The average dissipation rate from the cycling mode was approximately one order of magnitude larger than the value at constant depth, similar to the largest discrepancy in our observations. Ott et al. (2004) compared microstructure temperature measurements (Thorpe scale analysis only) from a towed undulating platform with vertical microstructure profiler measurements. The probability density functions of Thorpe scales indicated that those calculated from the vertical profiler were smaller in size. The comparison remained inconclusive, and the disparity was hypothesized to be attributed to natural variability. The pitch angle (20°–30°) of the towed undulating platform was comparable to our glider. Dissipation measurements using microconductivity sensors and fast thermistors have been made using similar undulating platforms (Dillon et al. 2003; Johnston et al. 2011).

f. Intermittency of turbulence

The intermittency of turbulence can be quantified using the variance of the natural logarithm of a turbulent variable, for example, for the dissipation rate, $\sigma^2_{\ln\varepsilon}$ (Gibson 1987). Using the 76 glider dive–climb cycles and the 90 VMP profiles (section 3), $\sigma^2_{\ln\varepsilon}$ and I_A are calculated. Figure 13a shows the intermittency factor averaged in 1°C bins. Typical intermittency factors in nature vary between 3 and 7 (Gibson 1987). At temperatures above 5°C, where the discrepancy between the VMP and the glider is observed, the intermittency factor in the glider data is substantially larger than the VMP data (Fig. 13a). In intermittent turbulence, an instrument is more likely to sample the remnants (''fossil'') of active patches (with small I_A) than sampling active (overturning) turbulence (Gibson 1987; Yamazaki et al. 1990). The dissipation measured by the VMP, at the upper IL and above, is therefore relatively smaller than

TABLE 3. The mle of the mean from a lognormal distribution, and mean of the lognormal distribution fit to the pdf of ε (W kg^{-1}). Results are for data conditionally sampled for T.

Method	$T < 3$°C	$3 \le T < 6$°C	$6 \le T < 9$°C
VMP-mle	3.3×10^{-7}	9.8×10^{-8}	3.3×10^{-9}
VMP-fit	4.1×10^{-7}	1.3×10^{-7}	4.0×10^{-9}
Glider-mle	3.3×10^{-7}	2.4×10^{-7}	3.9×10^{-8}
Glider-fit	5.2×10^{-7}	4.1×10^{-7}	7.4×10^{-8}

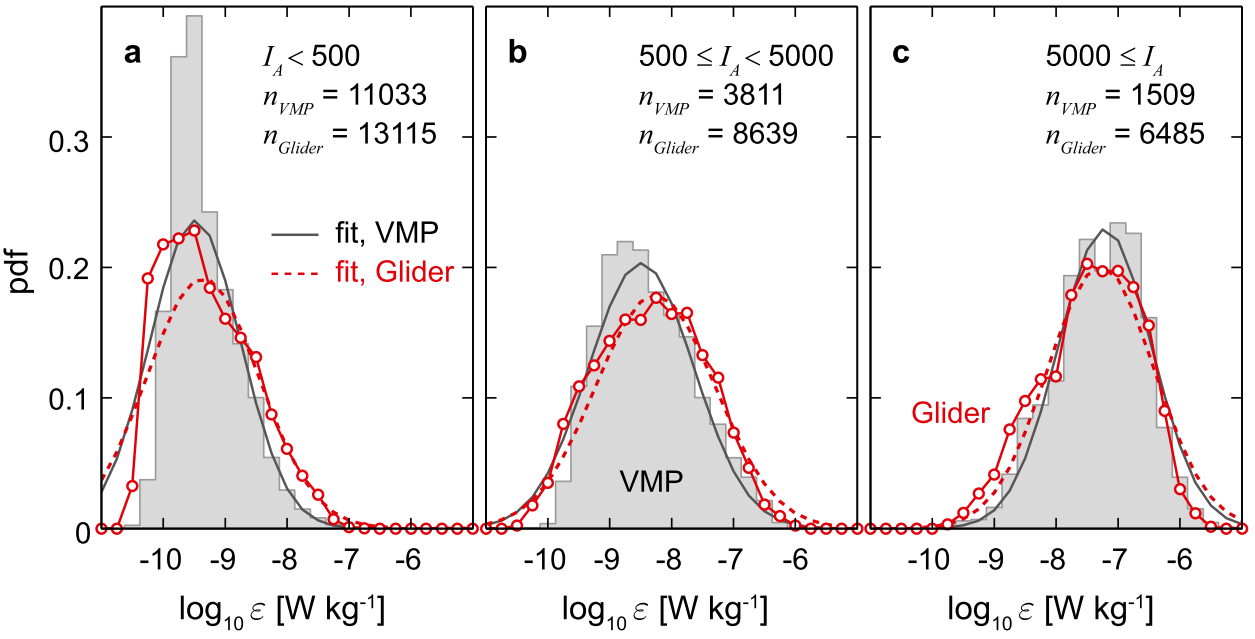

FIG. 12. As in Fig. 11, but conditionally sampled for the turbulent index I_A: (a) $I_A < 500$, (b) $500 \le I_A < 5000$, and (c) $5000 \le I_A$.

that measured by the glider. A pdf of the I_A with values less than 20, an approximate threshold for "fossil" turbulence (Gibson 1987), with respect to temperature supports this statement (Fig. 13b); that is, VMP samples relatively quiescent waters in temperature classes of 5°–7°C.

In each depth bin relative to the 3°C isotherm, the number of data points n averaged is in the range of 200–220 and 100–450 for the collocated VMP and glider profiles, respectively. We can estimate the accuracy for the expected value of ε with 95% confidence for given n and intermittency factor using Eq. (8) of Baker and Gibson (1987); see also the discussion by Gregg et al. (1993) on the results of Baker and Gibson (1987). We assume that $\sigma^2_{\ln\varepsilon}$ is approximately 6 for $T \ge 3$°C (i.e., for $z - z_{3C} \ge 0$) and 4 for colder water (see Fig. 13a), and further assume, arbitrarily, that one-half of the data points in each bin are independent, and take $n = 100$ for the VMP and $n = 200$ for the glider. We did not check the lack of correlation between the samples in the average profiles; however, our vertical averaging length scale of 15 m is comparable to the minimum averaging length of 10 and 15 m required for uncorrelated sampling found for the Patch Experiment (PATCHEX) and PATCHEX north data, respectively (Gregg et al. 1993). The expected value of ε is then measured to approximately 62% and 97% accuracy for the glider, and 97% and 161% for the VMP, below the IL and above the IL, respectively. The relatively poor accuracy (large percent values) for each instrument is because of the increase in the intermittency factor. The values of ε, however, vary by four orders of magnitude and accuracy within a factor of 2 is not unreasonable.

6. Summary

We measured the rate of dissipation of kinetic energy ε using a glider equipped with shear probes and using a vertical microstructure profiler (VMP). The measurements were made during the same cruise and sampled the turbulent plume of the Faroe Bank Channel overflow. A total of 76 dive–climb cycles from a 1-week mission of the glider, and 90 vertical profiles from the VMP were analyzed. Approximately one-half of the dataset was collocated with an average horizontal separation of 8 km. Each instrument sampled sufficiently over the dominant 3–4-day period variability at the site.

The glider velocity through water, the angle of attack, and ascent and descent angles are obtained from a hydrodynamic flight model (Merckelbach et al. 2010). After excluding the segments near the turning depth of the glider, and when the flow past the sensor (U) was not

TABLE 4. As in Table 3, but for data conditionally sampled for I_A.

Method	$I_A < 500$	$500 \le I_A < 5000$	$5000 \le I_A$
VMP-mle	1.4×10^{-9}	2.6×10^{-8}	2.7×10^{-7}
VMP-fit	1.4×10^{-9}	2.2×10^{-8}	2.8×10^{-7}
Glider mle	2.9×10^{-9}	4.7×10^{-8}	2.7×10^{-7}
Glider-fit	3.8×10^{-9}	6.5×10^{-8}	3.8×10^{-7}

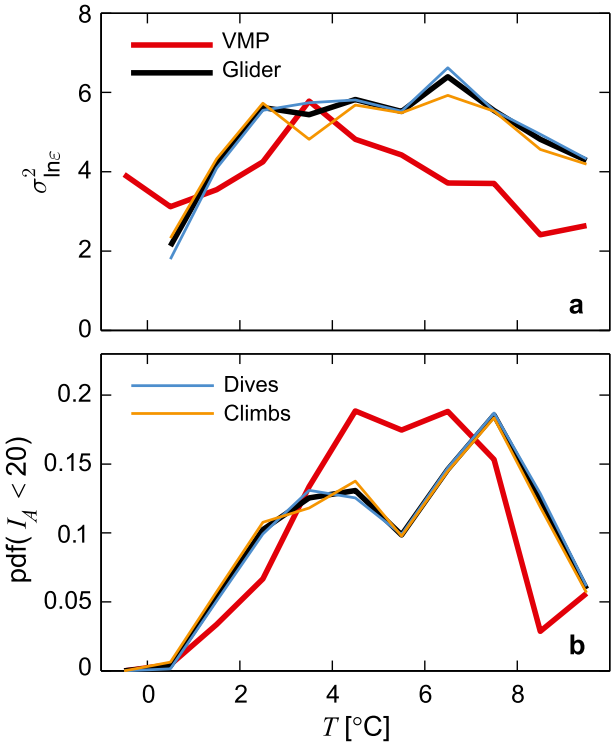

FIG. 13. (a) Intermittency defined as the variance of logε calculated in unit bins of T. There are only 10 dive (and no climb) data points from the glider for $T < 0$°C; these are excluded. (b) Pdfs of the turbulent activity index $I_A = \varepsilon/\nu N^2$, conditionally sampled for values < 20. Curves are for the VMP (red), the glider (dives and climbs together, black), and dives only (blue) and climbs only (orange).

sufficiently greater than an estimate of the turbulent velocity scale (u_t), we were left with about 67 700 dissipation measurements from the glider. The total number of data points from the vertical profiler was 29 000. The angle of attack (AOA) was sufficiently small, about 2°–4° during dives and 1°–2° during climbs, and allowed for high-quality shear probe measurements. The glider velocity through water was about 40 cm s^{-1} with typical ascent and descent angles of about 33° and 25°, respectively, from the horizontal.

The shear probe data were contaminated and unreliable for values of $R = U/u_t < 15$; the dissipation rate measurements from orthogonal probes differed by more than a factor of 10, and the AOA increased by one order of magnitude. The measurements were of high quality for the remaining data. The shape of the shear wavenumber spectra suggests that the lowest detection level in ε, $<5 \times 10^{-11}$ W kg^{-1}, is comparable to the best available vertical microstructure profilers. The effect of flow distortion near the sensors and the effect of rudder action in adjusting glider heading are both found to be negligible.

Averaged profiles of ε from the VMP and the glider agreed and differed in different parts of the water column and the overflow plume. The agreement in average dissipation in the turbulent bottommost 100 m, or for layers with temperature colder than 3°C (i.e., beneath the overflow plume interface), was better than 50%. Higher above, in the sheared and stratified interfacial layer (IL) of the overflow plume, the glider data substantially deviated from the VMP data, in average profiles, layer average values, and the probability distribution functions. The glider average values were approximately a factor of 3 and 9 times larger than the VMP values in the layers defined by 3°–6° and 6°–9°C, respectively. The vertical velocity and the speed of the glider showed large variance as the glider ascended and descended through the IL, and slowed down by approximately 15%. Compared to the vertical profiler, relatively slow mean vertical velocity and the slanted path of the glider led to substantially more horizontal sampling in the turbulent plume. We attribute the discrepancy to the different sampling scheme and the intermittency of turbulence. The intermittency factor calculated in temperature bins suggests that the glider dataset is up to a factor of 2 more intermittent than the VMP dataset in the IL. Despite large values of ε, because of the strong stratification, the turbulent activity index attains low values in the IL and above, and the VMP transects are likely biased toward measuring the ceasing, inactive turbulence. An examination of the probability distribution functions of ε conditionally sampled for different ranges of the activity index shows that the glider and the VMP datasets are drawn from the same population, at 95% confidence, for the values of the activity index larger than 500.

The glider offers a noise-free platform suitable for ocean microstructure measurements. Our measurements were collected from a site where the turbulent swift flow challenges the glider flight behavior. Nevertheless, we found that the dissipation measurements from the glider meet expectations and return data of sufficient quality suitable for studies of both ocean mixing processes and long-term monitoring and mapping of diapycnal mixing.

Acknowledgments. This work was funded by the Research Council of Norway, through the FRINAT program, under the Project 204867/V30, ''Faroe Bank Channel Overflow: Dynamics and Mixing.'' The authors thank Rolf Lueck, Gerd Krahmann, Lucas Merckelbach, Henrik Søiland, Webb Research glider support team, and the crew of R/V *Håkon Mosby*, students, and colleagues involved in the fieldwork. Comments from three anonymous reviewers and Shaun Johnston helped to improve an earlier version of the manuscript.

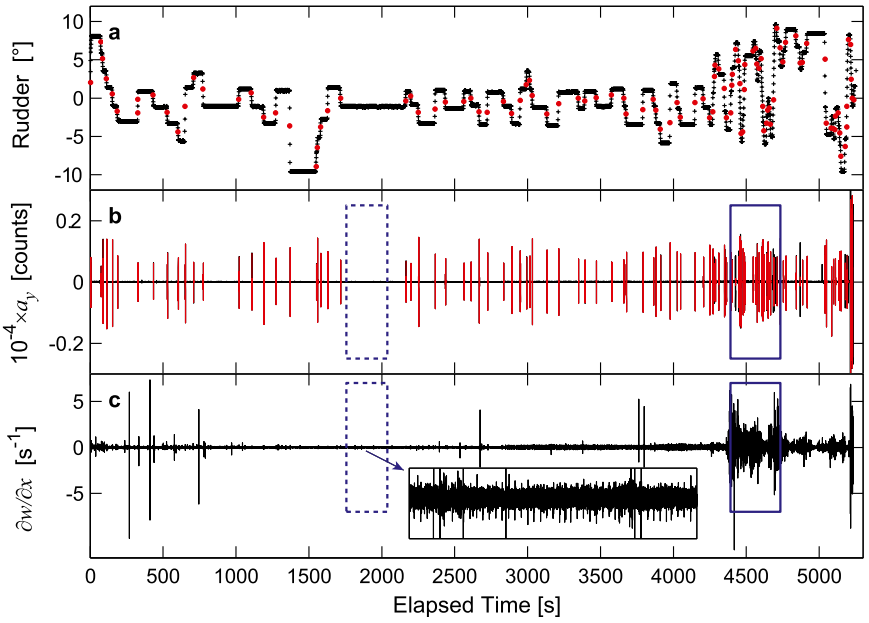

FIG. A1. Time series illustrating the influence of the rudder motion on the tail fin of the glider and the LED on MR. The time series is from the entire profile shown in Fig. 4. (a) Rudder angle measured by the glider's sensor. The red bullets mark the times of substantial rudder activity detected as described in the text. (b) Acceleration (raw data in counts) in the transverse y direction and (c) the shear probe signal recorded by probe 1. Shear data from probe 2 are very similar. Acceleration in the x direction is relatively less energetic.

APPENDIX

Noise Induced by the Rudder and Light-Emitting Diode

The influence of the rudder activity on the acceleration and shear probe data is illustrated using the dive profile, and the quiescent and turbulent segment examples of Figs. 4 and 5. Times of substantial rudder activity are detected as peaks of centered-first differenced rudder angles $> 0.3^\circ\,s^{-1}$. The time series of the rudder angle and the time of peaks (red bullets) are shown in Fig. A1a. The 50-m-thick quiescent and turbulent segments are marked in the figure; note the lack of rudder activity in the quiescent segment in contrast to the turbulent segment.

To infer acceleration and shear spectra representative of the times when the rudder is active, we extract 3-s-long segments of data centered at the detected peaks. In total, there are 110 peaks. The selected segments are marked in red in Fig. A2b. Each time the rudder is active, there is a clear signature on the a_y data. Its influence on the shear time series is masked by the high signal-to-noise ratio. The frequency spectra are shown in Fig. A2 for all 110 segments in pale color. For reference, spectra are also calculated for the entire 50-m segments of Fig. 5 (blue dashed: quiescent; thick blue: turbulent segment).

The acceleration in the direction along the axis of the instrument a_x is less energetic than a_y, as expected (Wolk et al. 2009). The a_y spectra show a small peak centered at 10 Hz, of equal amplitude, for both the turbulent and the quiescent segments. Because of the lack of rudder activity in the quiescent, this peak is likely not due to the rudder. The energetic segment shows additional peaks at 30, 60, 80, and 120 Hz, clearly associated with the rudder; the average spectrum (black) from the 110 instances of substantial rudder activity shows identical peaks.

The low-frequency portion of the shear spectra, used in dissipation rate calculations, is relatively uncontaminated by the rudder signature. The 110 segments (gray curves in Fig. A2b) have varying levels of energy; the energetic segments mask the peaks to as high as 80 Hz. The least-, average-, and most-energetic shear spectra are highlighted in black. Note that the spectrum from the turbulent 50-m segment is comparable to the most energetic curve, whereas the spectrum from the quiescent segment is about a factor of 10 more energetic than the spectrum with the minimum energy. The quiescent spectrum of Fig. 5a is one decade more energetic than the low-energy shear spectra presented in Fig. A2b.

Finally, the light-emitting diode (LED) on the MR induces spiking in the shear probe and temperature gradient time series (for reasons unknown), which is masked when the signal-to-noise ratio is high but is

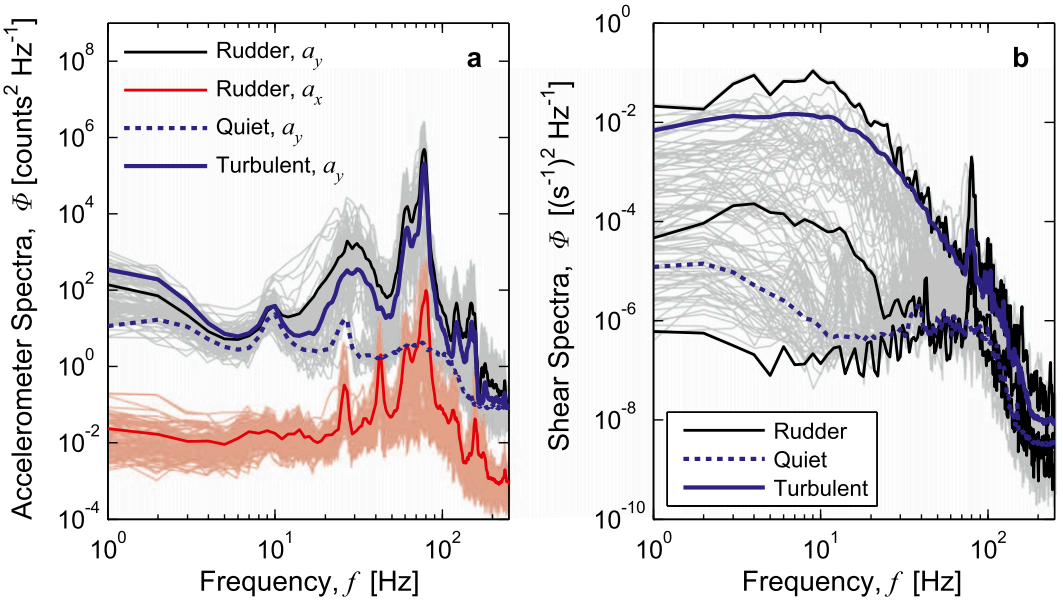

FIG. A2. Frequency spectra of (a) a_x (red) and a_y (black), and (b) shear $\partial w/\partial x$ for the segments shown in red in Fig. 14b. The spectra shown in pale colors are from all of the110 segments at each 3 s interval when the rudder was active. The average spectra are shown in thick black and red lines. The three spectra highlighted in (b) are those from the least-, average-, and most-energetic 3-s segments. Additionally a_y and shear spectra are shown from the 50-m-thick quiescent (dashed blue) and turbulent (thick blue) segments used in Fig. 5. Note that in the quiescent segment, the rudder was not active.

visible in quiescent segments of the data (see the inset in Fig. A1c). The LED blinks at 1-s intervals with the purpose of alerting the user that the instrument is on and acquiring data. This spiking has negligible, if any, influence on our dissipation rate measurements.

REFERENCES

Baker, M. A., and C. H. Gibson, 1987: Sampling turbulence in the stratified ocean: Statistical consequences of strong intermittency. *J. Phys. Oceanogr.,* **17,** 1817–1836, doi:10.1175/1520-0485(1987)017<1817:STITSO>2.0.CO;2.

Beaird, N., I. Fer, P. Rhines, and C. Eriksen, 2012: Dissipation of turbulent kinetic energy inferred from Seagliders: An application to the eastern Nordic seas overflows. *J. Phys. Oceanogr.,* **42,** 2268–2282, doi:10.1175/JPO-D-12-094.1.

Darelius, E., I. Fer, and D. Quadfasel, 2011: Faroe Bank Channel overflow: Mesoscale variability. *J. Phys. Oceanogr.,* **41,** 2137–2154, doi:10.1175/JPO-D-11-035.1.

——, J. E. Ullgren, and I. Fer, 2013: Observations of barotropic oscillations and their influence on mixing in the Faroe Bank Channel overflow region. *J. Phys. Oceanogr.,* **43,** 1525–1532, doi:10.1175/JPO-D-13-059.1.

Davis, R. E., C. C. Eriksen, and C. P. Jones, 2003: Autonomous buoyancy-driven underwater gliders. *Technology and Applications of Autonomous Underwater Vehicles,* G. Griffiths, Ed., Taylor and Francis, 37–58.

Dillon, T. M., J. A. Barth, A. Y. Erofeev, G. H. May, and H. W. Wijesekera, 2003: MicroSoar: A new instrument for measuring microscale turbulence from rapidly moving submerged platforms. *J. Atmos. Oceanic Technol.,* **20,** 1671–1684, doi:10.1175/1520-0426(2003)020<1671:MANIFM>2.0.CO;2.

Fer, I., G. Voet, K. S. Seim, B. Rudels, and K. Latarius, 2010: Intense mixing of the Faroe Bank Channel overflow. *Geophys. Res. Lett.,* **37,** L02604, doi:10.1029/2009GL041924.

Gibson, C. H., 1987: Fossil turbulence and intermittency in sampling oceanic mixing processes. *J. Geophys. Res.,* **92,** 5383–5404, doi:10.1029/JC092iC05p05383.

Goodman, L., E. R. Levine, and R. G. Lueck, 2006: On measuring the terms of the turbulent kinetic energy budget from an AUV. *J. Atmos. Oceanic Technol.,* **23,** 977–990, doi:10.1175/JTECH1889.1.

Gregg, M. C., H. E. Seim, and D. B. Percival, 1993: Statistics of shear and turbulent dissipation profiles in random internal wave fields. *J. Phys. Oceanogr.,* **23,** 1777–1799, doi:10.1175/1520-0485(1993)023<1777:SOSATD>2.0.CO;2.

Høyer, J. L., and D. Quadfasel, 2001: Detection of deep overflows with satellite altimetry. *Geophys. Res. Lett.,* **28,** 1611–1614, doi:10.1029/2000GL012549.

Johnston, T. M. S., D. L. Rudnick, G. S. Carter, R. E. Todd, and S. T. Cole, 2011: Internal tidal beams and mixing near Monterey Bay. *J. Geophys. Res.,* **116,** C03017, doi:10.1029/2010JC006592.

Jones, C., E. Creed, S. Glenn, J. Kerfoot, J. Kohut, C. Mugdal, and O. Schofield, 2005: Slocum gliders—A component of operational oceanography. *Proc. 14th Int. Symp. on Unmanned Untethered Submersible Technology,* CD-ROM, Durham, NH, Autonomous Undersea Systems Institute, 10 pp.

L'Heveder, B., L. Mortier, P. Testor, and F. Lekien, 2013: A glider network design study for a synoptic view of the oceanic mesoscale variability. *J. Atmos. Oceanic Technol.,* **30,** 1472–1493, doi:10.1175/JTECH-D-12-00053.1.

Legg, S., and Coauthors, 2009: Improving oceanic overflow representation in climate models: The Gravity Current Entrainment Climate Process Team. *Bull. Amer. Meteor. Soc.,* **90,** 657–670, doi:10.1175/2008BAMS2667.1.

Lueck, R. G., F. Wolk, and H. Yamazaki, 2002: Oceanic velocity microstructure measurements in the 20th century. *J. Oceanogr.,* **58,** 153–174, doi:10.1023/A:1015837020019.

MacKinnon, J. A., M. H. Alford, R. Pinkel, J. Klymak, and Z. Zhao, 2013: The latitudinal dependence of shear and mixing in the Pacific transiting the critical latitude for PSI. *J. Phys. Oceanogr.,* **43,** 3–16, doi:10.1175/JPO-D-11-0107.1.

Macoun, P., and R. G. Lueck, 2004: Modeling the spatial response of the airfoil shear probe using different sized probes. *J. Atmos. Oceanic Technol.,* **21,** 284–297, doi:10.1175/1520-0426(2004)021<0284:MTSROT>2.0.CO;2.

Merckelbach, L., D. Smeed, and G. Griffiths, 2010: Vertical water velocities from underwater gliders. *J. Atmos. Oceanic Technol.,* **27,** 547–563, doi:10.1175/2009JTECHO710.1.

Moum, J. N., M. C. Gregg, R. C. Lien, and M. E. Carr, 1995: Comparison of turbulent kinetic energy dissipation rate estimates from two ocean microstructure profilers. *J. Atmos. Oceanic Technol.,* **12,** 346–366, doi:10.1175/1520-0426(1995)012<0346:COTKED>2.0.CO;2.

Mudge, T. D., and R. G. Lueck, 1994: Digital signal processing to enhance oceanographic observations. *J. Atmos. Oceanic Technol.,* **11,** 825–836, doi:10.1175/1520-0426(1994)011<0825:DSPTEO>2.0.CO;2.

Nasmyth, P. W., 1970: Ocean turbulence. Ph.D. thesis, University of British Columbia, 106 pp.

Osborn, T. D., and R. G. Lueck, 1985: Turbulence measurements from a submarine. *J. Phys. Oceanogr.,* **15,** 1502–1520, doi:10.1175/1520-0485(1985)015<1502:TMWAS>2.0.CO;2.

Ott, M. W., J. A. Barth, and A. Y. Erofeev, 2004: Microstructure measurements from a towed undulating platform. *J. Atmos. Oceanic Technol.,* **21,** 1621–1632, doi:10.1175/1520-0426(2004)021<1621:MMFATU>2.0.CO;2.

Rudnick, D. L., R. E. Davis, C. C. Eriksen, D. M. Fratantoni, and M. J. Perry, 2004: Underwater gliders for ocean research. *Mar. Technol. Soc. J.,* **38,** 73–84, doi:10.4031/002533204787522703.

——, T. M. S. Johnston, and J. T. Sherman, 2013: High-frequency internal waves near the Luzon Strait observed by underwater gliders. *J. Geophys. Res.,* **118,** 774–784, doi:10.1002/jgrc.20083.

Seim, K. S., and I. Fer, 2011: Mixing in the stratified interface of the Faroe Bank Channel overfow: The role of transverse circulation and internal waves. *J. Geophys. Res.,* **116,** C07022, doi:10.1029/2010JC006805.

Simonsen, K., K. M. H. Larsen, L. Mortensen, and A. M. Norbye, 2002: A new bathymetry for the Faroe shelf. Tech. Rep. 2002-07, University of the Faroe Islands, 9 pp.

Smith, D. K., and D. Sandwell, 1997: Global sea floor topography from satellite altimetry and ship depth soundings. *Science,* **277,** 1956–1962, doi:10.1126/science.277.5334.1956.

Smyth, W. D., and S. A. Thorpe, 2012: Glider measurements of overturning in a Kelvin–Helmholtz billow train. *J. Mar. Res.,* **70,** 119–140, doi:10.1357/002224012800502381.

Thorpe, S. A., 2012: Measuring overturns with gliders. *J. Mar. Res.,* **70,** 93–117, doi:10.1357/002224012800502417.

Ullgren, J. E., I. Fer, E. Darelius, and N. Beaird, 2014: Interaction of the Faroe Bank Channel overflow with Iceland Basin intermediate waters. *J. Geophys. Res. Oceans,* **119,** 228–240, doi:10.1002/2013JC009437.

Wolk, F., H. Yamazaki, L. Seuront, and R. G. Lueck, 2002: A new free-fall profiler for measuring biological microstructure. *J. Atmos. Oceanic Technol.,* **19,** 780–793, doi:10.1175/1520-0426(2002)019<0780:ANFFPF>2.0.CO;2.

——, R. G. Lueck, and L. C. St. Laurent, 2009: Turbulence measurements from a glider. *Proc. OCEANS '09,* Biloxi, MS, MTS/IEEE, 6 pp. [Available online at http://ieeexplore.ieee.org/stamp/stamp.jsp?tp=&arnumber=5422413&isnumber=5422059.]

Wyngaard, J. C., L. Rockwell, and C. A. Friehe, 1985: Errors in the measurement of turbulence upstream of an axisymmetric body. *J. Atmos. Oceanic Technol.,* **2,** 605–614, doi:10.1175/1520-0426(1985)002<0605:EITMOT>2.0.CO;2.

Yamazaki, H., R. G. Lueck, and T. Osborn, 1990: A comparison of turbulence data from a submarine and a vertical profiler. *J. Phys. Oceanogr.,* **20,** 1778–1786, doi:10.1175/1520-0485(1990)020<1778:ACOTDF>2.0.CO;2.